A Novel Technique to Study Surface Profiles of Two-Dimensional Materials in LEEM

THESIS

submitted in partial fulfillment of the
requirements for the degree of

MASTER OF SCIENCE
in
PHYSICS

Author :	Arjo Andringa, BSc
Student ID :	s1286145
Supervisor :	Dr. ir. Sense Jan van der Molen
	Vera Janssen, MSc
2^{nd} corrector :	Prof. dr. Jan Aarts

Leiden, The Netherlands, December 11, 2017

A Novel Technique to Study Surface Profiles of Two-Dimensional Materials in LEEM

Arjo Andringa, BSc

Huygens-Kamerlingh Onnes Laboratory, Leiden University
P.O. Box 9500, 2300 RA Leiden, The Netherlands

December 11, 2017

Abstract

In this thesis we present and scrutinize a technique to reconstruct the surface profile of a sample using a low energy electron microscope (LEEM). This technique is added to the rich catalogue of surface analysis techniques available in LEEM. We demonstrate that the surface profile of a sample can be deduced from the local tilt angles. This is done by studying the change in diffraction pattern. The procedure is then applied to two samples: a flake of $MoTe_2$ that has a bump on it and a flake of $MoTe_2$ that has collapsed into a trench. We show that we can correct for lensing effects that are introduced due to a non-flat surface. In these samples we determine the local tilt angle with an accuracy of 0.3°.

Contents

Chapter 1

Introduction

1.1 Two-dimensional materials

We live in a three-dimensional world and are used to the materials around us also being three-dimensional. In 2004 though, a two-dimensional material was first isolated and characterized: graphene [1]. A two-dimensional material consists of a sheet of material with a thickness of only one atom. In figure 1.1 a schematic picture of such a material is drawn. Strictly speaking a material with a thickness of one atom does have a height, so it is not two-dimensional. The electronic and mechanical properties of a monolayer material do show the effects of the strong confinement in the z-direction. Such materials where predicted theoretically, but to actually isolate them was done never before 2004.

There are many special properties of such a material. Since it is very thin, it is also a lightweight material. It is exceptionally strong relative to the thickness: due to the strong bonds of atoms within the layer, there can be a lot of force exerted on a two-dimensional material before it breaks apart. Several ideas for applications based on the strength of the material have been put forward. Reinforcing plastics or other materials by mixing

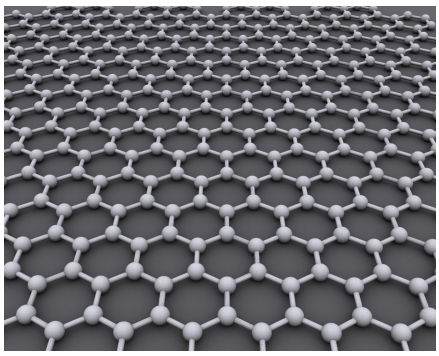

Figure 1.1: *Schematic picture of graphene, a two-dimensional material. The grey dots depict atoms and the rods the bonds in between the atoms. Reprinted from [2].*

graphene in has been proposed [3]. Another idea is to use graphene in space: using a graphene sail to propel a satellite by shining laser light on the sail has been suggested by Stephen Hawking [4].

Graphene also is an excellent conductor with an electron mobility that can exceed $15\,000\,\mathrm{cm^2V^{-1}s^{-1}}$ [5]. This opens the door to applications that are not yet feasible because smaller or thinner conductors are necessary. Due to the excellent conduction properties of graphene it can possibly be used as a very thin, flexible, and transparent component in electrical circuits [6].

1.2 Transition metal dichalcogenides

Most of these applications are still very far away, although a lot of research is being done on two-dimensional materials. Graphene is only the first of these materials we managed to isolate, many more exist. An example of other layered materials is the family of transition metal dichalcogenide (TMD) materials. TMD monolayers have a more complex structure than graphene, and their properties are also different. Graphene is not easy to make transistors of, since it has zero band gap, but TMD monolayers can have a band gap, which makes them interesting.

Another application of TMD monolayers is in the fabrication of thin devices. TMD monolayers can be semiconducting or metallic. This depends on the crystal structure, as shown in figure 1.2. The hexagonal 2H structure behaves as a semiconductor and the strained 1T' as a metal. The same material thus behaves as a metal or a semiconductor depending on the crystal structure. This opens up possibilities to mechanically change the electronic properties of the materials [7].

The switching between metal and semiconductor is interesting because contacting a semiconductor is difficult. There is a Schottky-barrier in a contact between a metal and a semiconductor, yielding a large resistance over the contact [8]. Having the contacted part of the thin device behave as a metal, would make the contact resistance much lower. The semiconductor-metal transition within the monolayer has been shown to not have this Schottky-barrier [9].

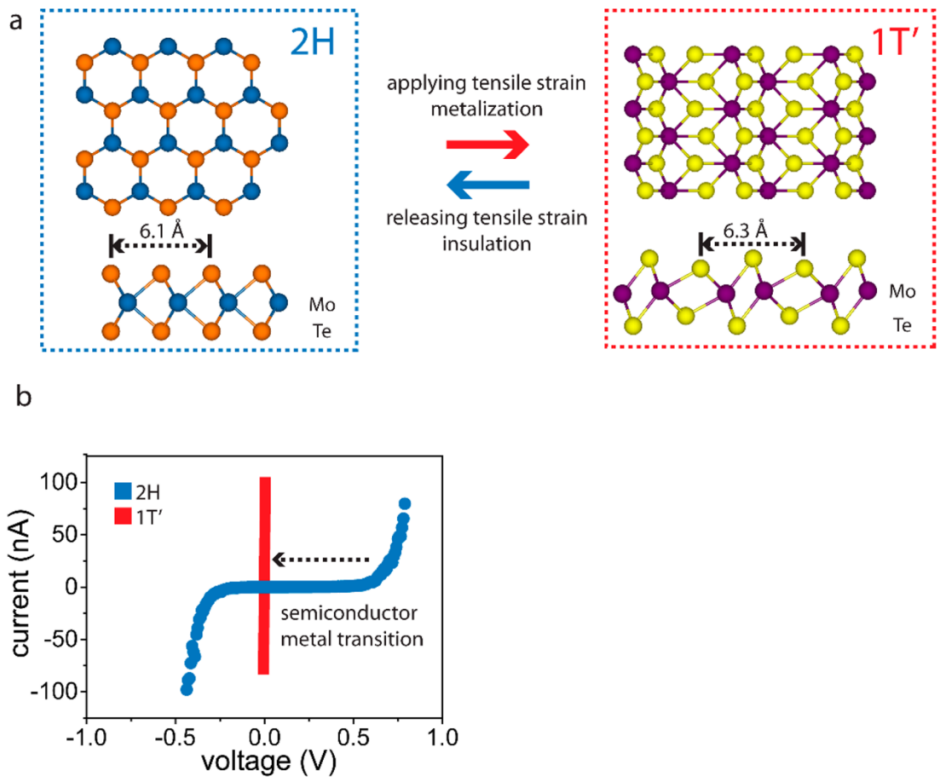

Figure 1.2: *a) On the left a TMD monolayer in a hexagonal, or 2H, crystal structure. On the right the strained, or 1T′, crystal structure. b) Current vs. voltage for a TMD monolayer in the 2H and 1T′ crystal structure. In the 2H crystal structure the material behaves as a semiconductor, in the 1T′ crystal structure as a metal. Adapted from [10].*

1.3 Measurements on two-dimensional materials

A way to study the switching of two-dimensional materials between being semiconducting and metallic, is to suspend them over a hole, forming a drum. In this way, so called 'freestanding' monolayers can be created. In figure 1.3 a diagram of this is sketched. Suspending a material makes it possible to look at the mechanical properties. Castellanos *et al.* used this structure to construct a mechanical resonator [11], but we want to use this design to induce strain in the monolayer. By pulling on the suspended part of the monolayer by capacative coupling, we want to bend the monolayer. This bending will strain the material. When the strain is large enough, we expect to observe the phase transition from the 2H to the 1T' crystal structure.

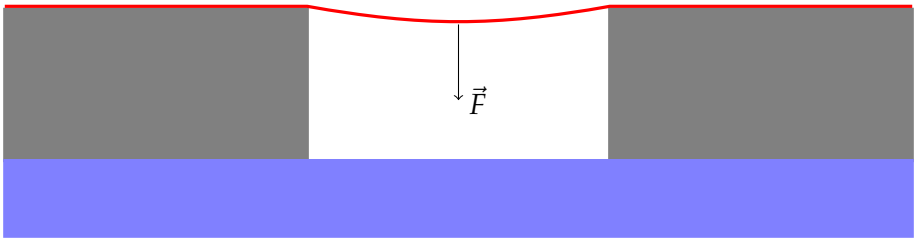

Figure 1.3: *Cut of a sample to induce strain in a monolayer. In red the monolayer and in blue the back gate that can be used to pull on the monolayer. The grey layer in between is an insulating substrate.*

The diameter of such drums is typically a few microns since it is difficult to create larger TMD monolayers. Such small structures are not easy to make, and not easy to do experiments on. Creating larger structures would be even harder though. Over the years, specific recipes to create samples with suspended monolayers have been developed. Still it often goes wrong and suspended parts of monolayers collapse into the holes they are suspended over. Understanding why and how this happens can help improve the existing recipes for fabricating samples.

1.4 Low energy electron microscopy (LEEM)

Studying the straining of drums and the structure of collapsed drums can be done in a low energy electron microscope. Using LEEM we are able to probe the crystal structure of a material. Electronic transport measurements can also be done. This makes LEEM a fitting method to study the straining of drums. What is still needed is a method to determine the deformation of the monolayer when there is a straining force on it.

For examining the structure of a collapsed drum we also need a method to probe the surface profile of a sample. In this thesis we will examine a

method that makes it possible to access information on the surface profile. It is not possible to directly see depth in a LEEM, but we can see if a part of a sample locally has an angle with the surrounding part of the sample. When we know the angles different parts of a sample relative to each other have, we can reconstruct the surface profile. In this way it is possible to gain knowledge of the structure of the sample in the third dimension.

Chapter 2

Low Energy Electron Microscopy (LEEM)

2.1 Introduction to LEEM

Analog to a standard optical microscope, a low energy electron microscope (LEEM) illuminates a part of a sample and then focuses the reflected image on the detector. The main difference with an optical microscope is that we use electrons instead of photons, which reduces the limit on resolution that is imposed by the wavelength of the particles. The lenses that are used are electromagnetic instead of glass-based. The lenses enlarge the illuminated field of view, which is typically in the order of a few micron, to see details down to a lateral resolution of 1.4 nm [12].

A low energy electron microscope uses electrons with an energy of less than 100 eV for imaging the surface of materials. The low energy of the electrons means that they have a low mean free path when interacting with a sample, which makes LEEM a relatively surface sensitive technique compared to other electron microscopy techniques such as scanning electron microscopy (SEM) and transmission electron microscopy (TEM). The penetration depth of the electrons in LEEM is a few atomic layers [13].

In figure 2.1 a schematic overview the LEEM instrument is shown. The electrons are emitted by the gun, in the top of the figure. In the gun the electrons are then accelerated to 15 kV. In this architecture the electron beam travels through the optics at 15 kV because the electron optics function better when using high energy electrons. A set of lenses focuses the beam before it enters the first magnetic prism array (MPA1, after this referred to as 'the first prism'). The first prisms bends the electron beam towards the sample. The beam is then focused on the sample by an objective lens.

The sample voltage is raised to -15 kV to decelerate the incoming electrons. We can then modify this -15 kV by a potential of up to 100 V to tune

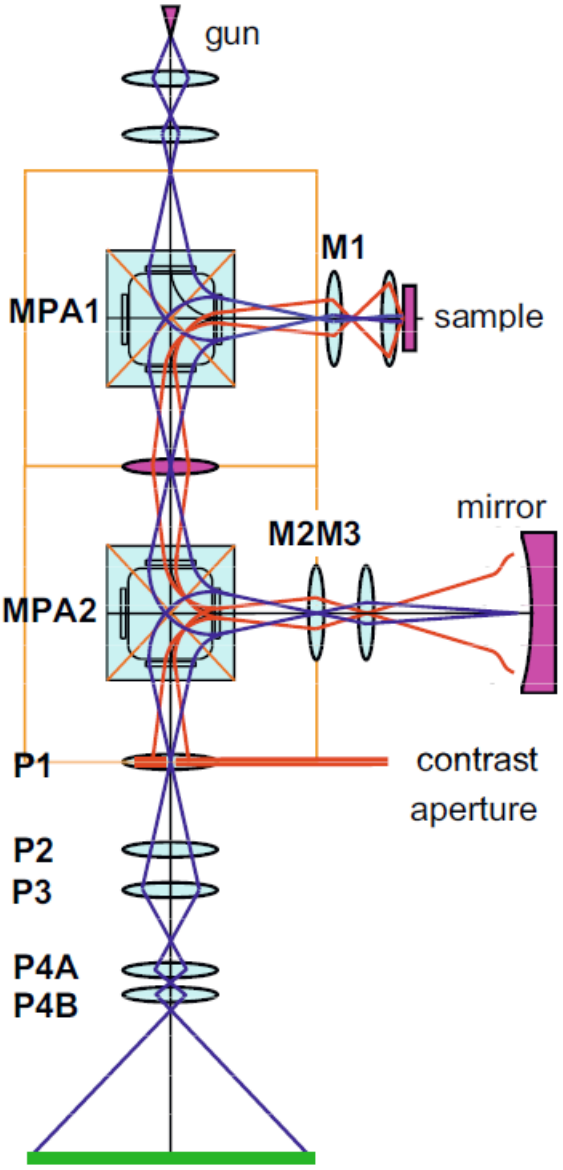

Figure 2.1: *An overview of the LEEM instrument. Reprinted from [14]*

the energy with which the electrons reach the sample. The reflected electrons are accelerated back to 15 kV. The objective lens focuses a diffraction pattern in the back focal plane of the lens, the real-space image is focused in the center of the first prism (MPA1). In figure 2.1 an image plane is located in the places where the red lines cross the optical axis, a diffraction plane is located in the places where the blue line crosses the optical axis.

The first prism bends the electron beam back into the projector column, where lenses P1-4 transfer the image to the detector (green in figure 2.1). Choosing between focusing the diffraction pattern or the real-space image on the detector is possible by turning lens P2 on or off.

2.1.1 Aberration correction

The objective lens introduces aberrations in the measured images. Electrons with different energies do not have exactly the same focal point (chromatic aberrations) and electrons that go through the objective lens near the edge of the lens are focused to a different point than electrons that go through the center (spherical aberrations). The aberrations are corrected by an electrostatic mirror. The electrostatic mirror is designed such that that the chromatic and spherical aberrations of the mirror are to the first order opposite to those of the objective lens. The opposite aberrations of the mirror effectively cancel the aberrations of the objective lens. This enhances the lateral resolution of LEEM from 5 nm to 1.4 nm [12][15].

The electrostatic mirror is introduced in the LEEM system by putting a second magnetic prism array in the projector column (MPA2). The second prism bends the electron beam to the mirror, and bends the reflected electron beam towards the detector.

2.2 Imaging modes

The LEEM can image in both real-space and diffraction as mentioned in section 2.1. These two methods can also be combined to do bright-field and dark-field LEEM. In real-space mode the reflected electrons are focused such that the image plane is on the detector. In diffraction mode the diffraction plane is focused on the detector.

2.2.1 Diffraction

Electrons that are reflected by a crystalline sample, are reflected under a specific set of angles only. These angles are determined by Bragg's law. Bragg's law states that waves need to constructively interfere when reflected from a crystalline lattice. The interference between the waves is

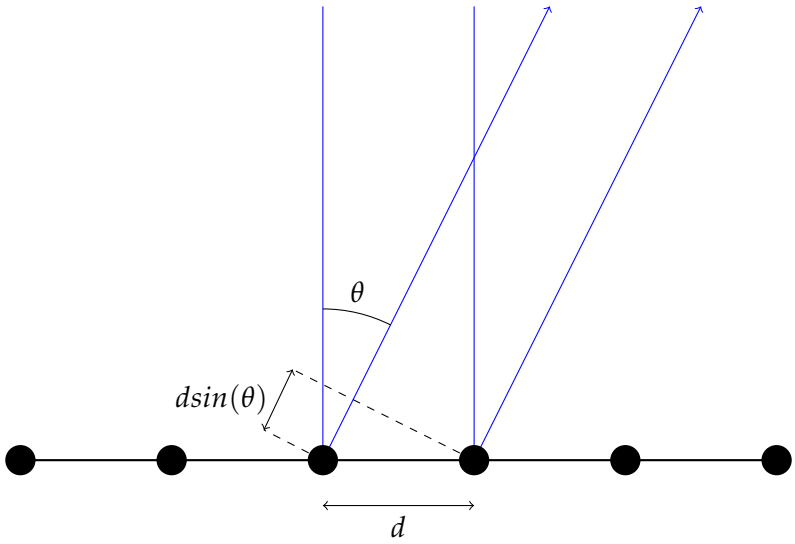

Figure 2.2: *Schematic drawing of Bragg's law. In blue the electrons that scatter of the lattice are shown. Constructive interference happens for all angles that yield a difference in the optical path length that is a multiple of the wavelength of the used wave, in our case electrons.*

determined by the angle with which the waves leave the sample. Mathematically this can be expressed as

$$dsin(\theta) = n\lambda, \tag{2.1}$$

with d the distance between two layers, θ the angle of the reflected waves and λ the wavelength. The reflected waves interfere constructively for a multiple of λ, which gives the n in equation 2.1. This process is drawn schematically in figure 2.2.

Applying this to LEEM, means that the electrons are reflected in certain angles. These angles are determined by the lattice structure of the material of the sample and the energy of the electrons. Instead of projecting the real-space image on the detector, we can image the angle distribution. The angle distribution is called the diffraction pattern. The reflected electrons go through the objective lens and a diffraction pattern is formed in the back-focal plane of the objective lens. This is illustrated in figure 2.3. The central spot in figure 2.3(b) corresponds to the electrons that were reflected with a 90° angle. The six spots around the central spot correspond to electrons that were reflected with with an angle corresponding to a path length difference of one wavelength. The back-focal plane can then be transferred to the detector by changing the projector column. This way of imaging is called low energy electron diffraction (LEED).

The distance between a point in diffraction space and the central spot corresponds to the the magnitude of the angle of the reflected electrons.

The direction in which a spot is located corresponds to the direction in which electrons are reflected. Two electrons can be reflected under the same angle, but in a different direction. This shows up in the diffraction pattern as two separate spots that are located at the same distance from the central spot, but in a different direction.

μLEED

The LEED procedure is normally done on the complete field of view of the LEEM. This is the illuminated part of the sample with a diameter of a few micron. In some cases the diffraction pattern of a smaller part of the sample is needed. This can be done by inserting an illumination aperture in an image plane. The illumination aperture can be moved to select a part of the sample down to a diameter of 200 nm to illuminate. The diffraction pattern that is then focused on the detector, is only formed by this smaller area on the sample.

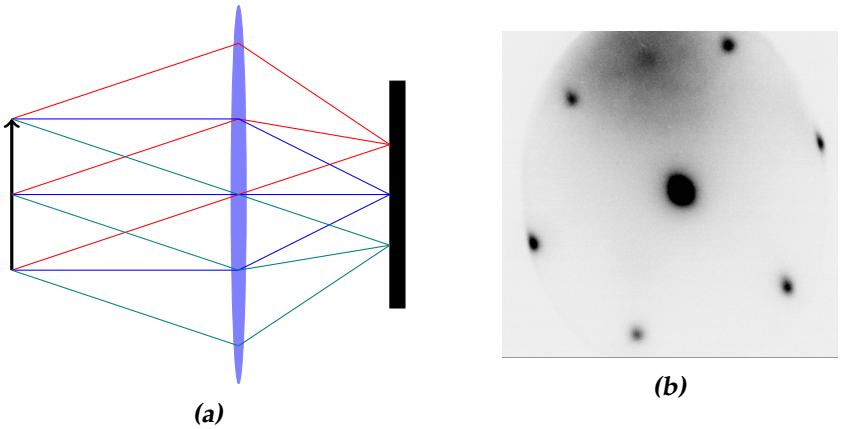

(a) ***(b)***

Figure 2.3: *a) Ray diagram of the way a LEED pattern is obtained. Electrons that leave the sample under a certain angle are focused in a plane and form a diffraction image. After that, the plane is transferred to the detector. b) Example of a diffraction image, in this case of $MoTe_2$. The middle spot corresponds to the blue lines in the ray diagram and is called the central of specular spot. The six surrounding spots correspond to the same angle of reflection, but in different directions and are called first order spots.*

2.2.2 Combining real-space and diffraction

One of the strengths of the LEEM is the possibility to combine real-space and diffraction information. There are not only apertures in image planes, but also in diffraction planes. Using the apertures in a diffraction plane, only those electrons leaving the sample with a certain angle can be selected.

By selecting for instance the central spot, the electrons that leave the sample with the angle of incidence are selected. This is called bright-field imaging. Focusing the real-space image on the detector then yields an image where height differences are accentuated since electrons destructively interfere at a step edge.

By selecting a non-central spot, the area on the surface that contributes to that spot can be imaged in real-space. This is called dark-field imaging and gives information on the lattice structure and -orientation on a sample.

Chapter 3

Angle determination using diffraction

For examining the surface profile of a sample a new method needs to be developed. The method we demonstrate here is based on measuring local tilt angles on a sample. From the local tilt the surface profile can then be reconstructed.

In section 2.2.1 it is shown that it is possible to image the angle distribution, or diffraction pattern, of the electrons that are reflected by the sample. Each diffraction spot is related to a certain angle. That the electrons make an angle with the surface, implies that the momentum of the electrons has an in-plane and an out-of-plane component. This is illustrated in figure 3.1(a).

When two parts of a sample are locally tilted with respect to each other, the tilt shows up in the image of the diffraction pattern. For purposes of clarity, we will call the orientation of the major part of the sample 'flat', and the usually smaller part with a different orientation 'tilted'. The electron microscope is aligned such that the electron beam reaches the flat part of the sample under an angle of 90°.

Tilt of a sample changes the angle with which the reflected electrons leave the sample. For the specular spot the angle of incidence is the same as the angle of refraction. For a flat surface this means that the electrons are reflected with an angle of 90° with the sample. However if the surface is tilted, the angle of incidence is no longer 90° and the electrons will not be reflected straight back. The angle the reflected electrons make with the incoming electron beam will be two times the angle the tilted part of sample makes. This is illustrated in figure 3.1(b). Note that an electron that is reflected under an angle with the electronic potential, will follow a parabolic trajectory. The electron is accelerated by the potential in the out-of-plane direction, but the in-plane momentum is constant.

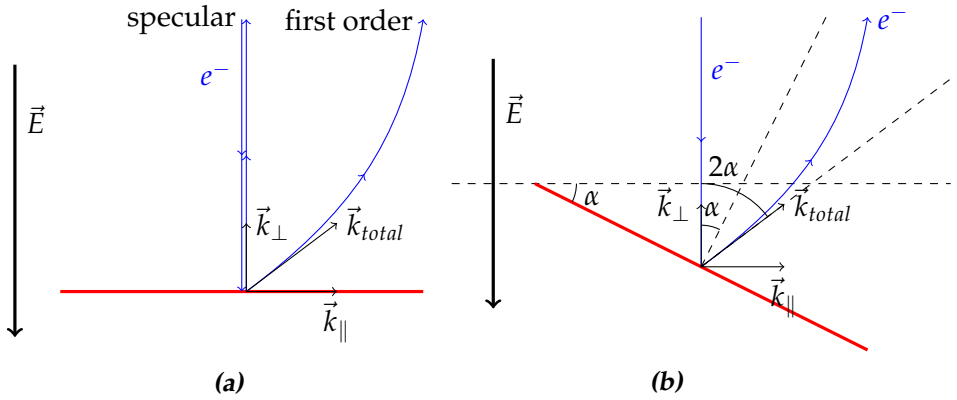

Figure 3.1: *a) Reflection of electrons on a flat sample. In blue the path of the electrons, in red the sample. Both the specular reflected electrons and the first order diffracted electrons are drawn. In black the momentum of the outgoing first order diffracted electrons, separated in in-plane and out-of-plane momentum. b) Reflection of electrons on a tilted sample. In blue the path of the electrons, in red the sample. Only the specular reflected electrons are drawn. In black the momentum of the outgoing electron, separated in in-plane and out-of-plane momentum.*

Since all electrons will be reflected with an angle that includes the tilt angle of the sample, the position in the diffraction plane where the diffraction pattern is focused will change. The relative angle differences between the diffraction spots will not change, since they are only dependent on the lattice structure of the material. Thus the diffraction pattern itself will stay the same, but the position it has in the diffraction plane will change. We will use the angle information in the diffraction planes now to gather information on the local tilt of the sample.

3.1 LEED pattern interpretation

The next step is to quantify the relation between the shift in diffraction space and the angle with which electrons leave the sample. This can be done using the diffraction spots of a flat part of the sample as a gauge.

The angle of the electrons is determined by the ratio between the out-of-plane momentum and the in-plane momentum. In figure 3.1(b) this ratio is illustrated for an electron that is reflected by a tilted part of a sample. The out-of-plane momentum is accelerated to 15 keV after the electron is reflected*, so effectively it is the in-plane momentum that determines the angle.

*This is not exactly true, since the out-of-plane momentum with which the electrons leave the sample is added to this 15 keV. The extra out-of-plane momentum is three orders of magnitude smaller than the 15 kV though, thus it can be neglected.

The in-plane momentum corresponding to the different diffraction spots can be calculated from the crystal structure of a material [16]. When we image a flat part of the sample, we can then calculate the angle with which the electrons that make up these spots leave the sample.

When determining angles, we can use the specular spot and the first order spots as gauge points. For both we can calculate the in-plane momentum, and thus the angle the electrons have with the surface. The space in between these points then needs to interpolated.

3.1.1 Gauging of diffraction space

To get an accurate interpolation of diffraction space, we measured the diffraction pattern of a Si(111) sample. The structure of the surface of silicon depends on the direction in which the surface cuts through the lattice structure of the silicon. This particular surface structure has periodicities on a scale seven times as big as the atom-atom distance. The extra periodicities show up in the diffraction pattern as seven spots in a row. In literature this is known as a 7x7 reconstruction.

These seven spots corresponding to the 7x7 reconstruction we can use to gauge diffraction space. In figure 3.2(a) the diffraction pattern of a clean Si(111) sample is shown. We know that the spots in between the central spot and the first order spots have equally spaced in-plane momentum [17]. An intensity profile of one of the rows of spots is shown in figure 3.2(b). The conversion from in-plane momentum to position in diffraction space is sample independent, so we can use the position of these spots in diffraction space as a gauge.

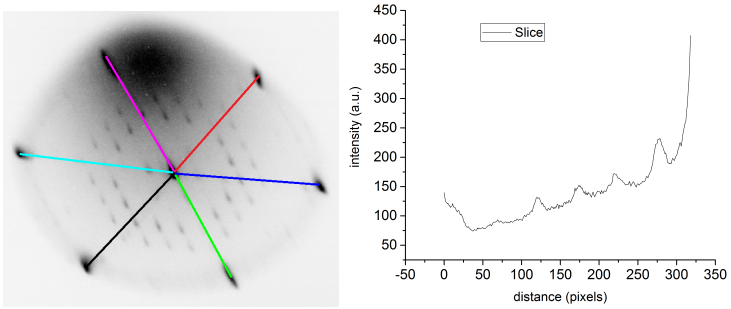

(a) ***(b)***

Figure 3.2: *a) The diffraction pattern of Si(111). Beneath the coloured lines are the spots corresponding to extra periodicities. The coloured lines correspond to the graphs in figure 3.3 in the same colour. Adapted from [18]. b) The intensity profile of the diffraction pattern along a straight line between the left first order spot and the central spot. Only the region in between the first order and the central spot is shown, the outer spots themselves are not included.*

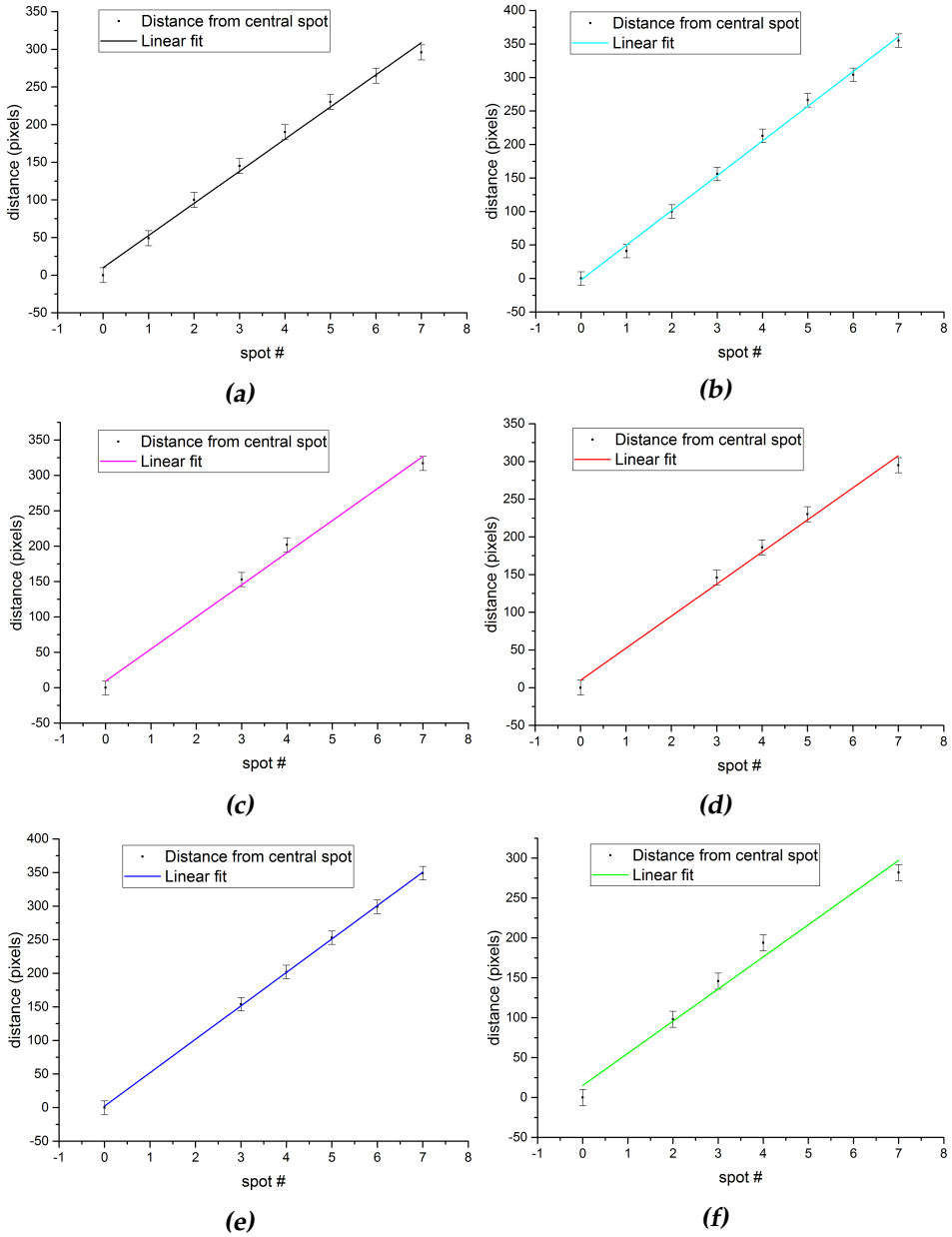

Figure 3.3: *The distance of the 7 diffraction spot from the central spot, for all six directions. The line colors correspond to the colors in figure 3.2(a).*

In figure 3.3(a) to figure 3.3(f) we show the distance between the central spot and the other diffraction spots, for the seven spots corresponding to the periodicities of the surface structure. This is done in six different directions. Linear fits are taken through the data points, and match well with the data points. In the following analysis we will thus use a linear dependency between distance in diffraction space and in-plane momentum.

3.1.2 Calculating tilt angles

Now we can derive a formula for the angle a material makes locally. In figure 3.1(b) α is the angle we want to calculate. Trigonometry gives us that

$$\alpha = \frac{1}{2} sin^{-1}\left(\frac{k_{\parallel}}{k_{total}}\right). \tag{3.1}$$

The momenta k_{total} and $k_{\parallel}$ are known. For k_{total} it is known that

$$k_{total} = \frac{\sqrt{2mE}}{\hbar}, \tag{3.2}$$

with m the electron mass and E the energy of the electron when it reflects of the sample. We can deduce $k_{\parallel}$ from the in-plane momentum of the first order spots of the material we look at. This yields

$$k_{\parallel} = \frac{r_{shift}}{r_{1storder}} k_{\parallel 1storder}, \tag{3.3}$$

with $r_{1storder}$ the distance between the central spot and the first order spot in diffraction space, and r_{shift} the distance between the shifted central spot and the position of the central spot in diffraction space for the flat areas. This is illustrated in figure 3.4. Here we use the linear distribution of in-plane momentum in diffraction space.

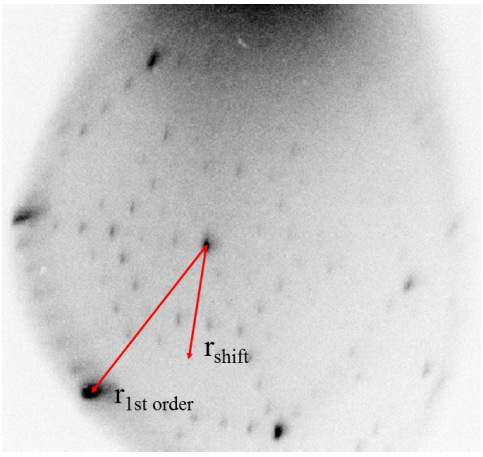

Figure 3.4: *Diffraction pattern with the distance between the central and first order spot ($r_{1storder}$) and the distance between the central spot and an example of where the shifted central spot could be (r_{shift}). Adapted from [18].*

Putting equations 3.2 and 3.3 in equation 3.1 now gives us

$$\alpha = \frac{1}{2} sin^{-1} \left(\frac{r_{shift}}{r_{1storder}} k_{\parallel 1storder} \frac{\hbar}{\sqrt{2mE}} \right). \tag{3.4}$$

This is the equation we will use to calculate the local tilt of area on samples, based on the shift of spots in diffraction space.

3.1.3 Direction of tilt angles

To examine the profile of the surface of a sample, not only the magnitude of tilt angles is needed but also the directions of the tilt angles. In figure 2.3 it is shown that opposite positions in diffraction space (the green and the red rays in the figure), correspond to opposite angles with which the electrons leave the surface. The correspondence between the angle that we see in diffraction space and the direction of the tilt is one-on-one: a 45° angle between the spot shifts in diffraction means a 45° angle between the directions of the tilt at the corresponding positions on the surface.

The absolute direction of the angles in real-space can not be deduced from measurements. The image in diffraction space shows differences between angles for different positions on the surface. In the imaging process in the LEEM there are rotations and flips of the image, that are different for real-space and diffraction images. To find the absolute direction, an idea of what the surface approximately looks like is needed. The measured relative angles can then be oriented in such a way that the angles correctly describe the surface.

3.2 Position determination of LEED spots

The accuracy of the calculation in section 3.1 depends on the accuracy of the position determination of a diffraction spot in diffraction space. Typically the highest point of a spot is called the center, and the center's coordinates the position of the spot. The accuracy of finding the position is dependent on the smoothness and size of the spot. Finding the center of a spot gets increasingly more difficult with spot size and spot roughness. An example is shown in figure 3.5. Figure 3.5(a) is an example of a relatively smooth spot where the position of the center is well defined, while the center of the spot in figure 3.5(b) is more difficult to determine. The error in the determination of angles as described in section 3.1 is mainly decided by the precision of the determination of the center of spots.

For all experiments presented in this thesis the position determination was done by hand. The procedure followed was to estimate by eye where a fit of the observed spot would have the peak. The position of the peak is then called the center. This is prone to errors, because chances are the point

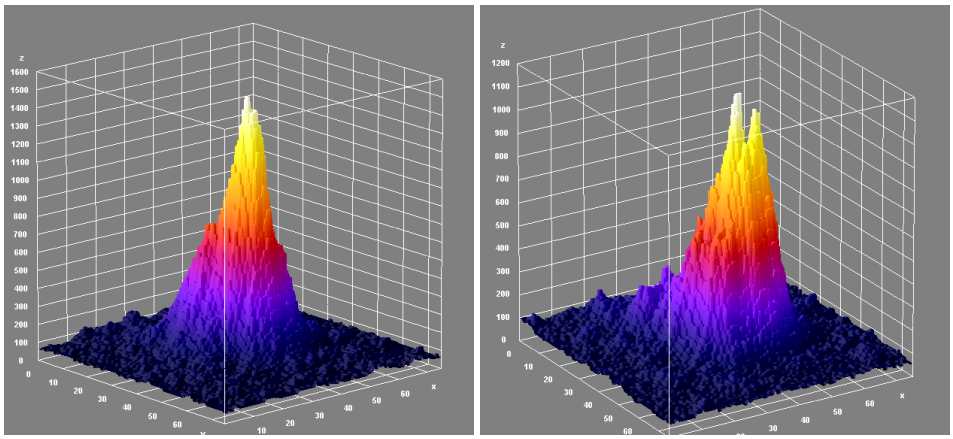

(a) **(b)**

Figure 3.5: *Examples of the profile of a) a smoothly shaped diffraction spot and b) a more roughly shaped diffraction spot.*

picked as the center of a spot will vary from person to person, especially when dealing with spots where the center is ill defined. It would be better to automatize this, because that makes the procedure more consistent. More on this will be said in the outlook.

Chapter 4

Improving resolution using deconvolution

The accuracy of the angle determination is limited by the resolution of determining the position of LEED spots. Especially for rough spots, the uncertainty in the position determination can grow to one fifth of the spot size. It might be possible to improve this resolution. The image that is seen on the detector is a convolution of the diffraction pattern created by the sample, and effects that are introduced because of imperfections in the LEEM. The effects of the imperfections in the LEEM combined are called the instrument response function (IRF). If it is possible to deconvolve these two parts of the image, we can improve the resolution of the position determination and with that the accuracy of the angle determination.

Mathematically the measured image can be expressed as

$$h = f \otimes g + n, \tag{4.1}$$

with h the measured image, f the true image, g the IRF, and n the noise. Here f contains the information we want to access. [19] By Fourier transforming the image a deconvolution can be performed, since a convolution in real-space is multiplication in Fourier space:

$$H = F \cdot G + N, \tag{4.2}$$

$$H/G = F + N/G, \tag{4.3}$$

with H, F, G and N the Fourier transforms of h, f, g and n respectively.

The practical feasibility of this technique depends on our knowledge of the instrument response function and the amount of noise in the measurement. If there is a lot of noise, the noise term in 4.3 can become larger than the image term. When the IRF that is used in the deconvolution differs from the actual IRF, parts of the resulting image can blow up.

A positive side effect of the deconvolution could be that the resolution improves enough to make it possible to see the information on the surface smoothness that is in a spot. The profile of a spot contains information about the smoothness of the surface and defects that are on it [20], but at the moment our resolution is not good enough to see this. If the resolution improves by the deconvolution, this information might become accessible. A possible issue here is the resolution of our measurements. The typical spot size in our current diffraction patterns is approximately 50 pixels. If the size of a spot is drastically reduced, there might be not enough pixels left to access the information on the surface structure.

In this section we will try to come as close to the IRF as we can and perform the deconvolution. If we succeed in this it will enhance the precision with which we can determine the position of diffraction spots and thus enhance the resolution of the angle determination.

4.1 The Instrument Response Function

The instrument response function (IRF) of a measurement instrument is defined as the output the instrument gives when the input is a delta peak. In the context of diffraction patterns, the input is the diffraction pattern as the sample produces it. For an infinite crystalline sample without defects the pattern consists out of delta peaks for every allowed reflection angle. The output is then the measured diffraction spot. Thus the IRF of the LEEM is the measured diffraction spot when the input is a delta function, or a perfectly sharp spot. The shape that is measured in such a case, is provided exclusively by the instrument and is thus the IRF.

This can be measured. By looking at the shape of the gun spot without interaction with the sample, we image the effects of the LEEM. This is called 'mirror mode'. In mirror mode, we make the (negative) potential on the sample a little bigger than the energy of the incoming electrons. This means that just before the electrons reach the sample, they are reflected back. In mirror mode the electrons travel through the complete instrument, but without interacting with the sample. The delta peak input is then the specular reflection of all electrons. The shape of the spot that is measured then, contains all the effects of the instrument.

The gun spot in mirror mode, measured in diffraction mode, is shown in figure 4.1(b). The spot is shaped ellipsoid, where the short axis is labeled in blue and the long axis in black. This measurement of the gun spot is used as the IRF to perform the deconvolution, or g in equation 4.1.

In figure 4.1 the result of the deconvolution operation is shown. Equation 4.3 is applied, using the measurement of the gun spot in mirror mode as the IRF. The resulting image shows a larger intensity at some of the positions of the diffraction spots, but others are no longer visible. The resulting

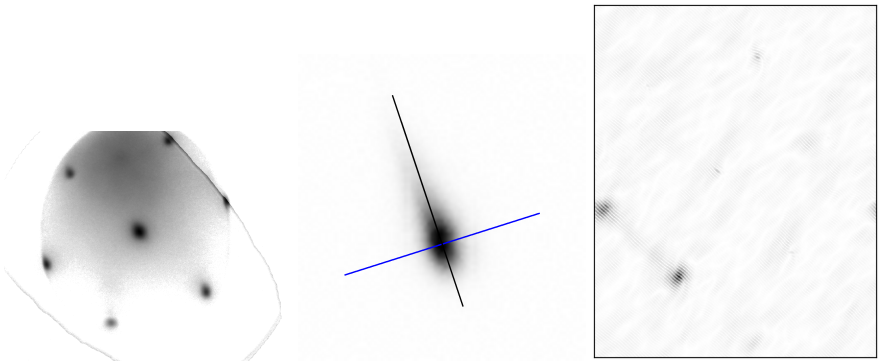

(a) **(b)** **(c)**

Figure 4.1: *a) A measured diffraction pattern. Contrast is inverted for clarity, the darkest spots have the highest intensity. b) The gun spot in mirror mode, measured in diffraction mode. This picture is enlarged for clarity, in reality the spot size is comparable to the spot sizes in figure 4.1(a). The spot is shaped ellipsoid, where we call the blue line the short side and the black line the long side. c) The result of deconvolving the diffraction pattern in figure 4.1(a) using the gun spot in mirror mode as the IRF.*

image also has a lot of noise and extra periodicities. There are two possible reasons for this: either the noise term N/G is too big, or the G we use here is not correct.

If the noise term is too big, the deconvolution will simply not work. But if the problem is the IRF, it might be possible to solve this. The disadvantage of measuring the IRF is that there also is noise in the measurement. The noise in the measurement of the IRF leads to the IRF that is used in the deconvolution being not exactly the IRF of the instrument, but the IRF plus noise.

Another way to get to the IRF is to look analytically at the shape the IRF should have. This shape can then be fitted on a measurement of the gun spot in mirror mode and be used to construct a mathematical model for the spot. This model is then the input for the deconvolution, and hopefully the noise can be eliminated that way. This will be discussed in the next two sections.

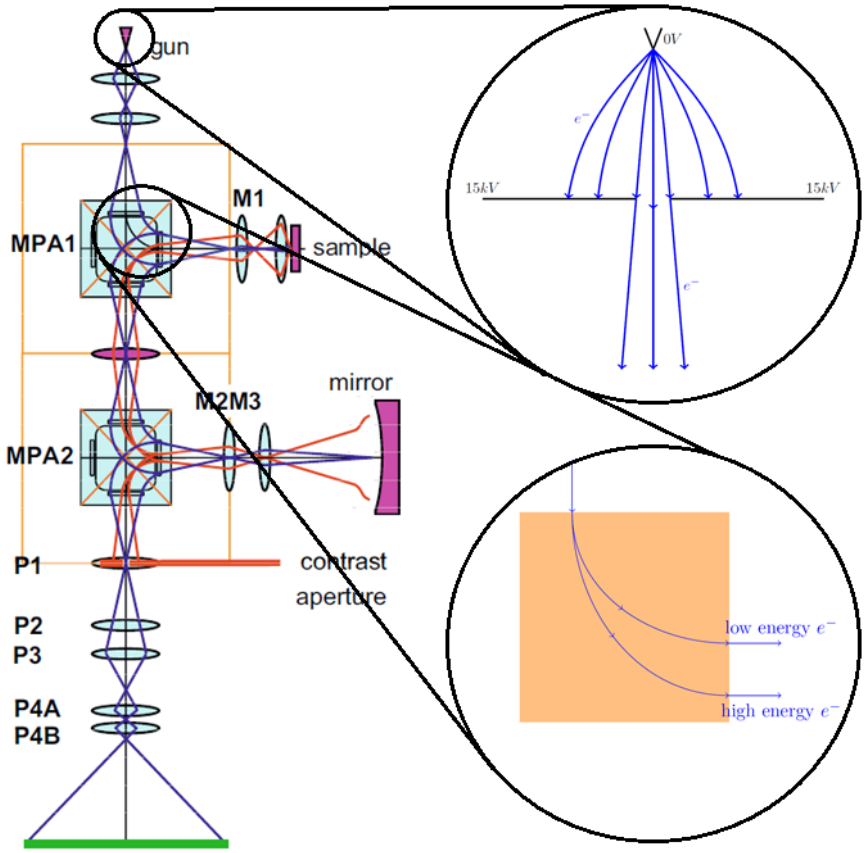

Figure 4.2: *Diagram of the set up of the LEEM. The electrons start in the top of the picture, when the are emitted by the gun. They travel down and via both arms until they reach the detector in the bottom. The upper inset depicts the working of the electron gun, the lower set in the effect of the magnetic prisms on the electron paths. Adapted from [14].*

4.2 Non-parallel extraction

To make a model of the gun spot the elements of the LEEM that contribute to the shape of the IRF need to be found. There are two main factors: the electrons do not leave the gun exactly parallel, and the electrons do not have exactly the same energy. The electron gun emits an electron beam that is not exactly parallel, which introduces a broadening of the diffraction spots. When the electrons do not have exactly the same energy, the prisms stretch the diffraction spots. In figure 4.2 these elements are highlighted. By calculating the effect of these two factors, we can calculate the shape of the IRF.

We first look at the non-parallel extraction of electrons out of the gun tip because an angle is a displacement in diffraction space. Diffraction spots are broadened because of this non-parallel extraction since the diffraction image displays the angle distribution of the reflected electrons. The goal is to find a mathematical description of the resulting distribution that is seen in diffraction space. This mathematical description can then be used to construct a model spot.

The upper inset in figure 4.2 shows the design of an electron gun. The exact details of the electron gun we use are not publicly known, but the general principle of an electron gun is. The type of gun that is used is a cold emission gun. Cold emission means that the gun is not heated. Heating the electron gun is often done to make extraction of electrons more easy. A side effect of heating is a larger spread in the energy of the electrons, which is an unwanted side-effect.

In a cold emission gun there is a sharp metal gun tip above an extractor plate. Between the extractor plate and the gun tip there is a potential difference, which is called the extraction voltage. The extracted electrons are accelerated towards the extractor plate. There is a small circular aperture in the extractor plate, which transmits a part of the electrons to create a parallel beam. The gun tip needs to be exactly above the aperture in the extractor plate for this procedure to work [21].

4.2.1 Checking the alignment of the gun tip

We can check whether or not the gun tip is correctly aligned above the aperture. When the prisms are turned off, the electron beam goes straight through the LEEM without interacting with the sample or the mirror. In figure 4.2 this would mean the beam would go directly from the gun tip at the top of the picture to the detector plate at the bottom. The beam can then be focused on the detector and should give a perfectly round spot. This round spot is under the assumption that the alignment of the lenses that are in between the gun and detector is perfect.

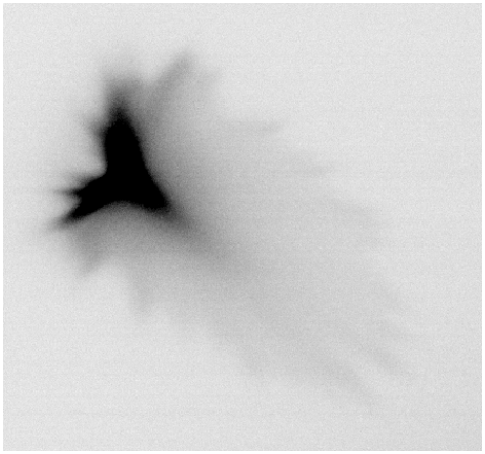

Figure 4.3: *Image of the electron beam, directly focused on the detector with the prisms turned off. Contrast is inverted for clarity, the darkest spot has the highest intensity.*

In figure 4.3 the image of the focused beam is shown: it is not round but ellipsoid. There are two possible causes for this. It is possible that the gun tip is not exactly above the aperture in the extractor plate, but shifted. This would stretch the spot in one direction. On the other hand it could also be that somewhere in the system the alignment was not perfect. The threefold symmetry in the brightest part of the spot is because there are aberrations in the electron optics. A large part of the aberrations gets corrected as described in section 2.1.1, but this is not the case for threefold symmetric aberrations. Our lenses are octopole magnets, so the lenses do not have the correct symmetry to correct threefold symmetric aberrations. This would require for instance a dodekapole magnet.

It is not clear whether or not the aberrations in the gun alignment will show in the measurements. When there are distortions in the measurements, it is a good idea to realign the gun.

4.2.2 Calculation of the spot profile

Now we can calculate the broadening of diffraction spots due to the beam being non-parallel. By transmitting only a small part of the emitted electrons through the aperture in the extractor plate, a nearly parallel electron beam is achieved. By accelerating the electrons to 15 keV the beam is made even more parallel. Nonetheless, there will still be some variation in the angle with which electrons come through due to the size of the aperture. To look at the intensity for different angles that come through, we do trigonometric analysis.

We want to know the distribution of angles with which electrons go through the aperture. In the paraxial approximation $sin(\theta) = \theta$ the distri-

bution in θ is proportional to the distribution of position where the electrons go through the aperture. In figure 4.4 this is illustrated: for small θ, θ and x are proportional.

This gives an approach to calculate the distribution of electrons. Let x be the distance from the center of the aperture and d the distance between the center of the aperture and the gun tip, then

$$r = \sqrt{d^2 + x^2}, \tag{4.4}$$

is the distance between a point in the aperture and the gun tip. The intensity of a point source as a function of distance in three dimensions follows

$$I \sim 1/r^2, \tag{4.5}$$

so the intensity as a function of distance from the center of the aperture (x) can be expressed as

$$I \sim \frac{1}{d^2 + x^2}. \tag{4.6}$$

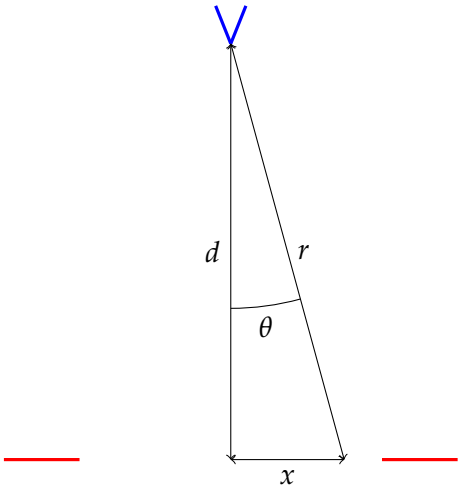

Figure 4.4: *The distance determination between a point in the aperture and the gun tip. The gun tip is drawn in blue, the extractor plate in red. The opening between the two parts of the extractor is the aperture, with d the distance between the tip and the center of the aperture, x the distance between the center of the aperture and the point where we want to know the intensity and r the distance between the point in the aperture and the gun tip. θ Is the angle between r and d.*

The broadening of the spot should also follow this relation. In this derivation we have assumed that the gun tip acts as a point source and that the electrons go in a straight line from the gun tip to the extractor plate. To check if the broadening of the spot indeed follows equation 4.6, we can fit the equation to a slice of the gun spot in mirror mode. As explained in section 4.1, the gun spot in mirror mode is approximately the IRF of the LEEM. It contains the broadening of diffraction spots caused by the non-parallel electron beam as described above, and the stretching of spots due to energy dispersion in the prisms. By taking a slice through the short side of the spot as described in figure 4.1(b), only the broadening effect is taken into account, not the stretching.

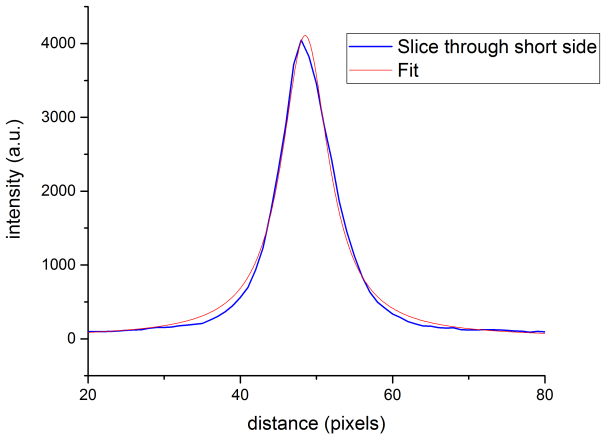

Figure 4.5: *In blue the profile of the gun in mirror mode. The slice was taken through the short side of the spot. In red a fit of equation 4.6 on the data.*

In figure 4.5 the result of fitting equation 4.6 on the slice is shown. There is a slight disagreement between the data and the equation. The assumptions that the gun tip is a point source and that the electrons go in a straight line are probably the cause for this disagreement. Still the equation does describe the slice of the gun spot in mirror mode quite closely. The equation is thus appropriate to use to describe the shape of the IRF as a first try. Is is possible though to improve here by taking into account the shape of the gun tip and the path of the electrons.

This slice is one-dimensional, but the result can be extrapolated to a two-dimensional shape. The x in figure 4.6 can be taken as distance from the center of the aperture in two dimensions. Taking the x in two dimensions translates to a two-dimensional image by rotating the fit in figure 4.5 around the peak of the fit. The result is then a two-dimensional shape that describes the broadening of the diffraction spot due to the non-parallel electron beam.

4.3 Energy dispersion

The next step is to look at the effects of the energy dispersion of the electrons when they are emitted. Also here the goal is to find a mathematical description that can be used to construct a model spot. The distribution in diffraction space is caused by the prisms in the LEEM that deflect the electrons based on their energy. The distribution can be seen in the long slice through the gun spot in mirror mode, shown in figure 4.1(b).

As described in section 2.1 LEEM has two prisms that deflect the electron beam. The first prism bends the electron beam to the sample, the second prism bends the electron beam to the aberration correcting mirror. The

prisms of the LEEM deflect the electron beam by applying a magnetic field. The magnetic field is perpendicular to the direction of the deflection. The Lorentz force then deflects the electrons that go through the magnetic field. This means that electrons with varying energies get scattered and stretch the electron beam in the direction of the deflection. This is largely compensated for in the system, but not entirely. The intensity distribution in the resulting, stretched spot is directly correlated to the energy distribution in the electrons when they enter the prism. In figure 4.2 there is an overview of the whole system. The lower cut-out shows the energy dependent scattering of electrons in the prisms.

The origin of the energy distribution is in the electron gun. The emitted electrons all have approximately the same energy, but not exactly. Fowler-Nordheim theory describes what the energy distribution should look like.

It can be calculated what this spread in energy looks like. According to SPECS, the manufacturer of our LEEM, the spread in energy is about $300meV$, but they do not specify what form the spread takes. For a cold emission gun, the energy spread is described by cold field emission theory, and already in 1928 Fowler and Nordheim published about this [22].

In a cold emission gun, the electrons are emitted by applying an extraction voltage on the gun tip. This potential enables the electrons to tunnel out of the gun tip into the surrounding vacuum. This process is drawn schematically in figure 4.6.

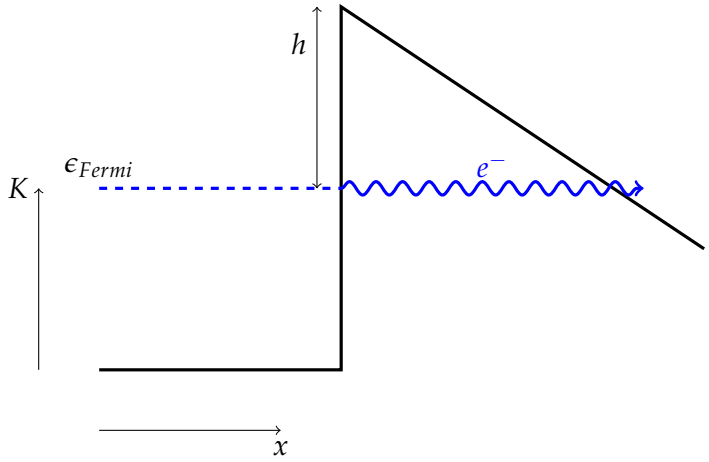

Figure 4.6: *Schematic image of the electron extraction in a cold emission gun. The potential in which the electrons move is drawn in black. On the x-axis is the distance in the direction perpendicular to the surface of the emitter, on the y-axis kinetic energy relative to the bottom of the conduction band of the emitter. The dotted blue line indicates the Fermi-level inside the emitter. The wiggly blue line is the electron tunneling through the potential barrier at the surface of the emitter. The height of the barrier as seen by the electrons on the Fermi surface is called h.*

There are two effects that now determine the energy dispersion of the emitted electrons. The electrons that are available for tunneling have an energy distribution that is described by the Fermi-Dirac distribution. The probability of the electrons tunneling out of the gun tip goes exponentially with energy. The equation that describes the spread in energy is

$$j(\epsilon) = z_S f_{FD} \frac{2F}{3b\phi^{1/2}} \exp\left(\frac{b\phi^{1/2}(3\epsilon/2 - \phi)}{F}\right), \tag{4.7}$$

with z_S Sommerfeld's electron supply constant, f_{FD} the Fermi-Dirac distribution, F the field gradient used to extract electrons from the gun tip, ϕ the work function of the gun tip and ϵ the energy of the electrons relative to the Fermi energy. Furthermore the constant $b = \frac{4\sqrt{2m}}{3e\hbar}$ with m the electron mass and e the electron charge. The derivation of equation 4.7 is shown in appendix A.

In figure 4.7 equation 4.7 is plotted. The tunneling transmission goes exponentially with energy. The energy dispersion will then be a balance between the Fermi-Dirac distribution - which declines with energy - and the exponentially increasing transmission probability. For electron energies bigger than the Fermi energy the transmission is limited by the Fermi-Dirac distribution and eventually goes to zero, for energies lower than the Fermi energy the transmission is limited by the tunneling probability and also goes to zero.

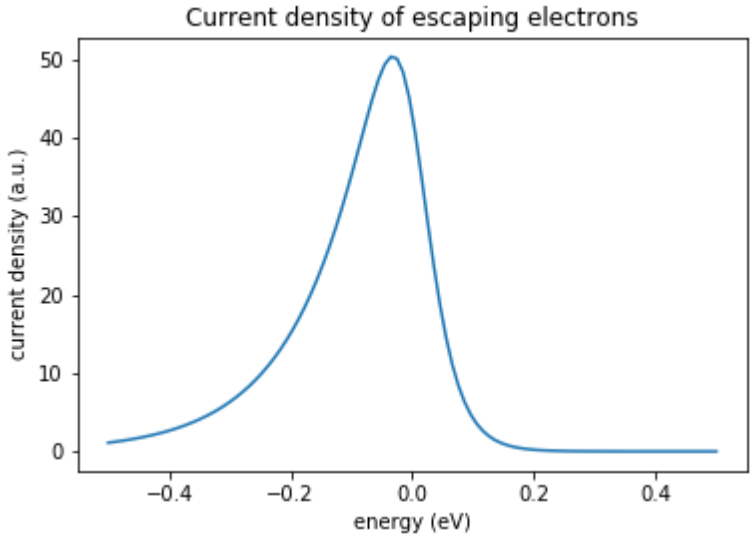

Figure 4.7: *The current density of escaping electrons as a function of the electron energy as described by equation 4.7. Values used are $\phi = 4.5eV$ since that is the work function of tungsten, $F = 1V/m$ and $T = 300K$.*

To make sure that equation 4.7 describes a distribution that goes to zero in both the positive and negative extremes, values for the constants need to be chosen that are not realistic. In the case of figure 4.7 we chose the field gradient to be 1 V/m. This is not corresponding to reality, since the extraction voltage typically is around 3000 V, while the size of the complete gun is in the order of 10 cm. These values would lead to a field gradient of hundreds of volts per centimeter.

The explanation for this the assumption that our gun is a flat surface that is big enough to use periodic boundary conditions in calculating the density of states. This assumption is very strong, and probably quite wrong since an electron gun tip is made very sharp. The diameter of a gun tip can be in the order of 10 nm. This leads to incorrect values for the constants in equation 4.7. Especially the field gradient at the surface of the gun tip will be influenced by the different surface structure. To see whether or not the shape of the distribution describes reality though, it can be compared to the shape of the IRF.

4.3.1 Comparison to the measured distribution

Now the result can be compared to the actual spot shape that is seen in diffraction patterns. The energy dispersion translates to a distance in diffraction space since the prisms scatter the electrons based on their energy. Electrons with different energies will thus have slightly different angles when interacting with the sample. Imaging this in diffraction mode gives a stretching of the diffraction spots in one direction. Just as in section 4.2, the function we get out of the analysis is fitted to the gun spot in mirror mode. The gun spot in mirror mode is approximately the IRF of the LEEM, so this gives an idea whether or not the analysis is correct.

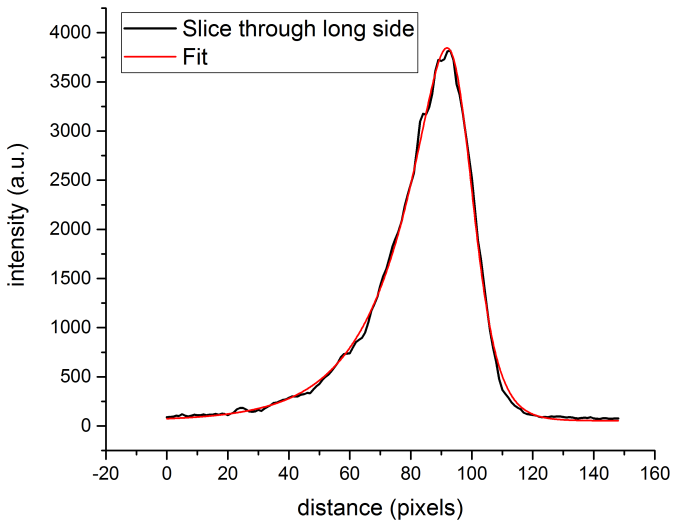

Figure 4.8: *In black the profile of the gun spot in mirror mode, taken through the long side. In red equation 4.7 is fitted on the data.*

In figure 4.8 a slice of the gun spot in mirror mode along the direction of the stretching is plotted. This is the long axis in figure 4.1(b). That means that the effect of the prisms is visible in this direction. Equation 4.7 is fitted on the slice of the gun spot in mirror mode, and matches the data very well. From this similarity we can conclude that equation 4.7 indeed describes the stretching of the gun spot due to scattering by the prisms. It can also be concluded that the approximations that were made (taking the shape of the potential barrier as a triangular barrier, Taylor-expanding the Gamow exponent $G(h)$ and the WKB-approximation) are good approximations in this case.

It can be concluded that we have accurate equations for the shape of the IRF, both for the short side and the long side of the spot as it is seen in mirror mode. That means these equations can be used to make a model spot, which can then be used in the deconvolution.

4.4 Model spot

Using equations 4.7 and 4.6 a model IRF can be constructed. The broadening in diffraction caused by the non-parallel beam (equation 4.6) describes a two-dimensional distribution. This two-dimensional distribution is convolved with the one-dimensional distribution caused by the energy dispersion (equation 4.7). The result is the model IRF.

Numerically this is done by padding the one-dimensional equation with zeros to give it the same shape as the two-dimensional equation. This model spot can then be used to deconvolve the IRF out of our measured diffraction images.

In figure 4.9 the model IRF is compared with the measured gun spot in mirror mode. The images of the spots given in figures 4.9(a) and 4.9(b) are barely distinguishable, and by comparing the slices in figures 4.9(c) and 4.9(d) we can see that they indeed describe the same shape, but the model is more smooth. The smoothness should make the deconvolution easier since it describes the IRF more precisely than the measured gun spot in mirror mode.

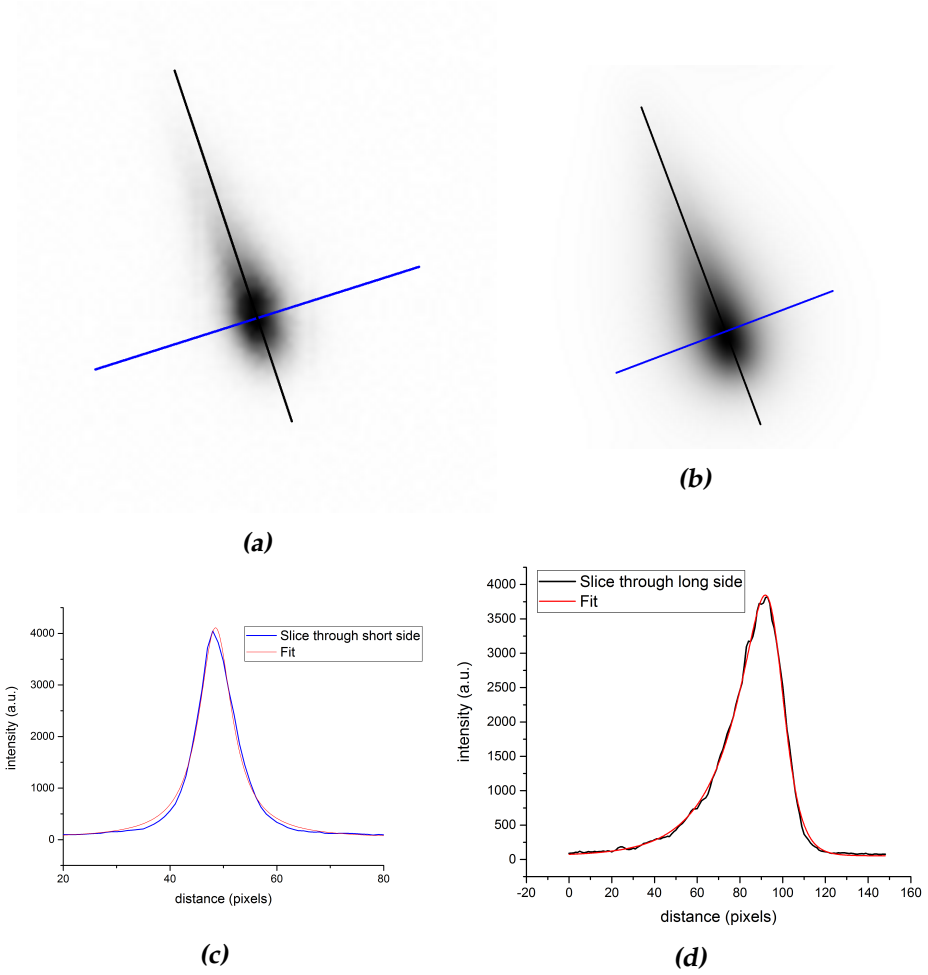

Figure 4.9: *a) The measured gun spot in diffraction mode. The electron beam was reflected without interaction with the sample, so called mirror mode. b) The model spot constructed with equations 4.7 and 4.6. c) Slice through the short side of both spots, indicated with black in (a) and (b) of this figure. In blue the slice of the measured spot, in red the slice of the model spot. d) Slice through the long side of both spots, indicated with black in part (a) and (b) of this figure. Here in black the slice of the measured spot, in red the slice of the model spot.*

Chapter 5

Applications of angle determination in LEEM

In chapter 3 it is shown that measuring angles in a LEEM can be done. The procedure was tested on two different samples. One sample had a flake of $MoTe_2$, transition metal dichalcogenide (TMD) put on a substrate of Si(100). The flake was meant to be suspended over a trench, but collapsed into it. This is an interesting situation to look at, since collapsing flakes happen more often in the fabrication of samples. Understanding why and how the collapsing happens can help improve the recipes used to produce samples.

The other sample is also a flake of $MoTe_2$. It is not suspended, but was put on top of a substrate that has a micro-particle on it. This made the flake bend over the micro-particle, creating a bump on the material.

5.1 Profile of a bump

5.1.1 Sample

To test the angle measurement procedure, an approximately ten layer thick flake of $MoTe_2$, put on top of a silicon substrate was imaged. A silicon wafer is used as starting substrate. On top a layer of silicon oxide is formed by exposure to air. A flake of $MoTe_2$ is then exfoliated from a crystalline piece of $MoTe_2$. The flake is transferred to a polymer stamp and the stamp is used to carefully transfer the flake to the silicon substrate. The resulting sample is shown in figure 5.1

In figure 5.3 we see an image of a part of the flake. The white spot is defocused, which means that that part of the sample is a bit higher than the surrounding part. Since there is a height difference, there should also be tilted areas around this defocused part of the flake. In the rest of this section, we will refer to this defocused part of the flake as the 'bump'.

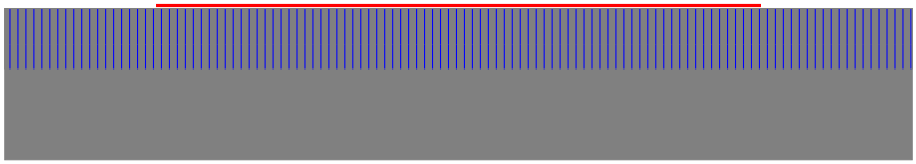

Figure 5.1: *Schematic image of the sample as it is prepared. In gray the silicon substrate, blue lines indicate the oxidized part. In red the flake of $MoTe_2$.*

The cause for the bump is most likely a micro-particle that was still on the silicon substrate when the flake of $MoTe_2$ was put on top of it. Such a micro-particle would push the flake slightly up and cause the defocusing on the bump. This is illustrated in figure 5.2. It is possible that the actual cause is something different, but the main point is that it is likely to find tilted parts on this sample.

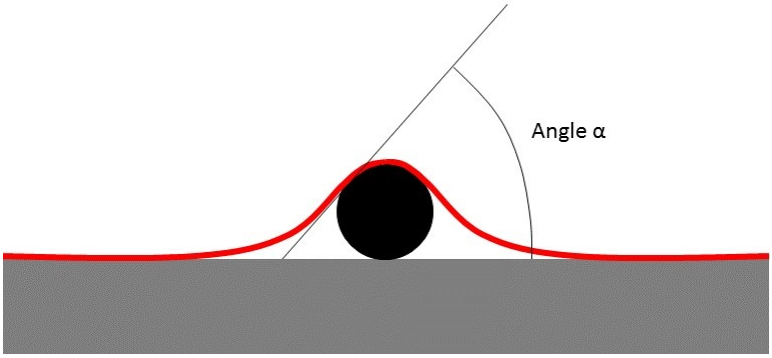

Figure 5.2: *Schematic image of the reason there is a bump on the flake of $MoTe_2$. The flake is shown in red, the silicon substrate in gray and the micro-particle in black. The image is not to scale.*

5.1.2 Measurement

In a LEEM it is possible to look at the diffraction pattern of a part of a sample down to 200 nm. This can be done by putting a plate with an aperture in the electron beam. By choosing the position of the aperture, only the electrons coming from a certain part of the sample can be selected.

This way, different parts on the bump can be selected. In section 3 it is shown that a tilted part of the sample shifts the diffraction pattern with respect to the original position. The angles that the material locally makes with the flat surface can be studied by looking at the shift of the diffraction pattern when it is taken on different parts of the bump.

In figure 5.3 a real space image of the $MoTe_2$ flake is shown. The positions where we illuminate the flake using an aperture are marked with a

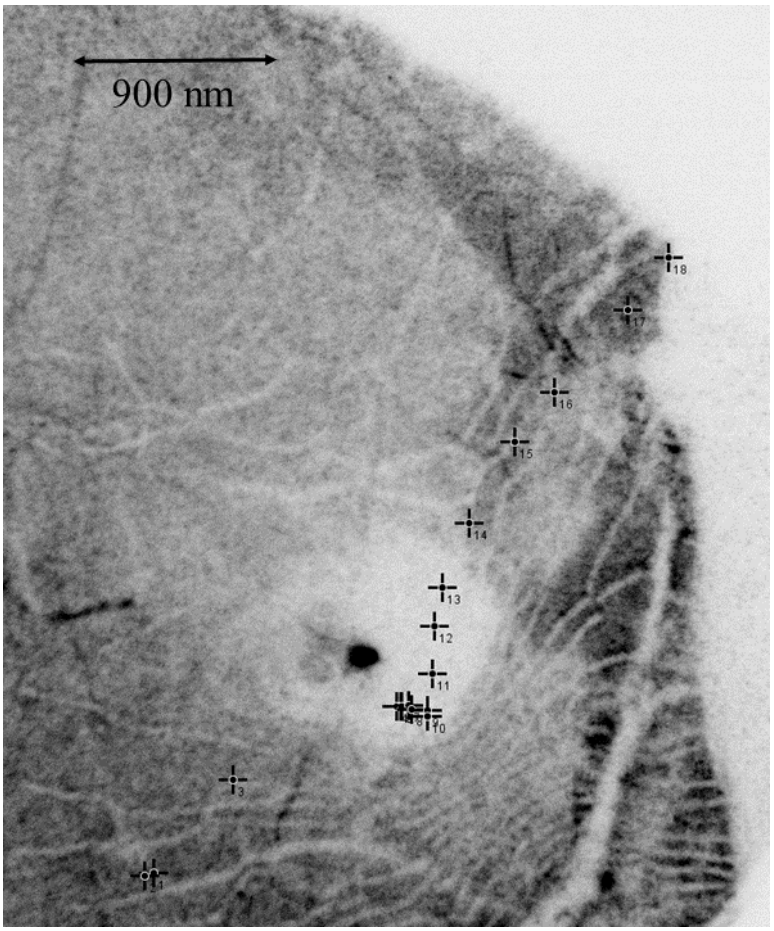

Figure 5.3: *Real-space image of the part of the sample with the bump on it. The crosses indicate the positions at which a diffraction image was taken, with the size of the crosses the size of the illuminated part of the sample.*

cross. For each of these positions the position of the specular spot is determined. The position of the specular spot in the position marked 1 is taken as the gauge for a flat part.

5.1.3 Results

We expect the specular spots from the diffraction pattern on the bump to be shifted with respect to the one that is not from a diffraction pattern on the bump. This is visible in the measurements. The central diffraction spot follows the track indicated in the inset of figure 5.4(b) clockwise when we go through the positions on the sample.

In figure 5.4(b) the position of the specular spot corresponding to all positions of the aperture is indicated on the background of the position of the spot in the flat situation. For this figure the spot corresponding to position 1 is selected to represent the flat situation. Two things are apparent: the distance the spot has moved from the flat situation changes, and the direction in which it has moved changes.

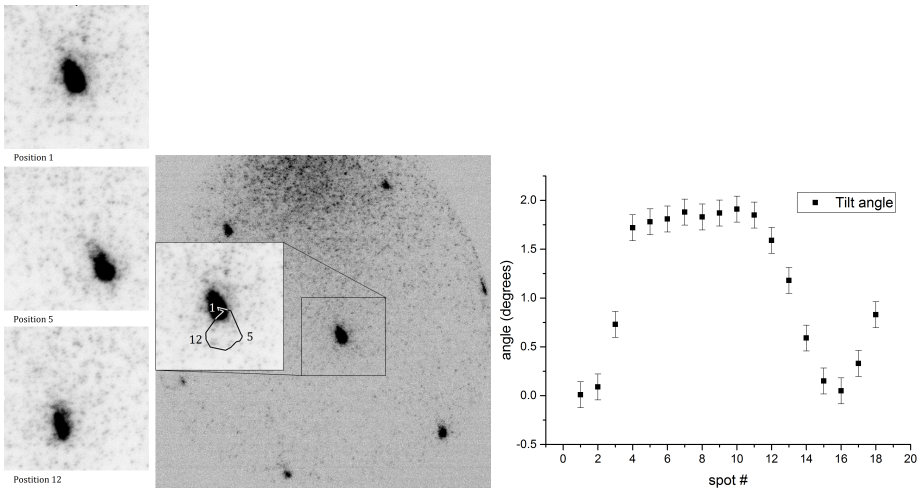

Figure 5.4: *a) Examples of the position of diffraction spots for different places on the sample. The x- and y-axis are gauged equally for all three images to show the shift of the spot. b) The diffraction pattern of the $MoTe_2$ flake. The inset shows the movement of the central diffraction spot when we go through the positions on the flake. The numbers correspond to positions on the flake. c) The angles of the tilt of the sample at the different positions on the flake.*

The distance the spot has moved directly corresponds to the magnitude of the angle the material makes with the flat surface. In figure 5.4(c) these angles are plotted for all positions of the aperture. Indeed it can be seen that for the middle positions in the graph, which are on the bump, the angle is bigger than on the side parts of the graph, which correspond to flat parts of the sample next to the bump. In the middle there is no dip in the magnitude of the angle, because all positions are taken on the side of the bump. The top of the bump would be expected to also be flat, but there were no measurements taken on the top of the bump.

Direction of angles

The direction in which the spot has moved corresponds to the direction of the tilt angles of the surface. As described in section 2.2.1 we need an approximate idea of the structure of the surface to determine the absolute directions of tilt angles. In this case we know that the highest part of the bump should be the defocused, white spot. From that it can be concluded that the angles should approximately be in the direction of the top of the bump.

In figure 5.5 the angles between the horizontal direction in diffraction space and the direction in which the spot has shifted are plotted. Comparing these angles with the positions on the surface where the diffraction

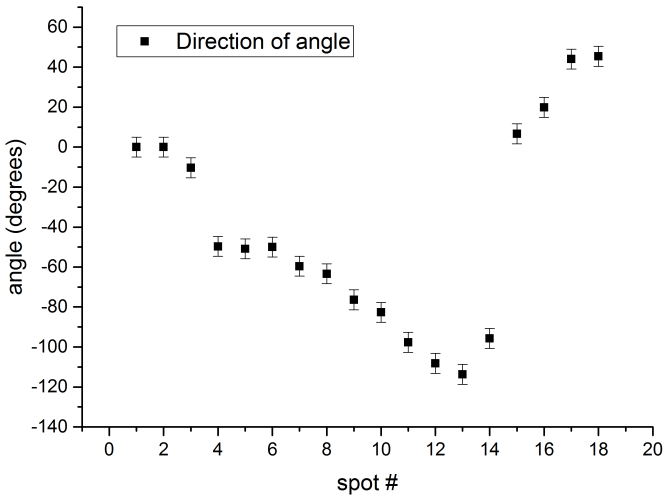

Figure 5.5: *The directions of the local tilt for the different positions on the flake. The angles are defined relative to each other, so have only meaning with respect to each other. The absolute direction needs to be determined with help of the knowledge of the sample.*

picture is taken shows a clear correspondence. At position four both the tilt angle and the angle of the direction change. In figure 5.3 it is shown that position four is the first position that is on the bump.

Positions three to 14 show a tilt angle with the rest of the sample surface in figure 5.4(c). In figure 5.6 the directions of the tilt angles are shown in the real-space picture, in such a way that they describe a slope towards the defocused spot. The direction of the angles relative to each other is measured, the choice of which direction is 0° is interpretation.

Constructing the surface profile

Doing these angle measurements on a surface, gives a vector field of angles. When the resolution of the measurements is good enough, the surface profile can be deducted from this vector field. In figure 5.6 it is apparent that that is not possible for this measurement. To construct the surface profile, the angle of the surface between two points where a diffraction surface is taken is needed. In the figure it can be seen that the direction of the angles do not connect two points. Since it is not possible to connect two points, we also can not determine the profile of the surface in between. For that it would be needed to do these angle measurements in a grid over the bump, or in a line that by chance lines up with the direction of the angles.

To do this in a reliable way, the points where the angle is measured should not be much further apart than the size of the position we measure. For the aperture we used to select a part of the surface, this is 200 nm.

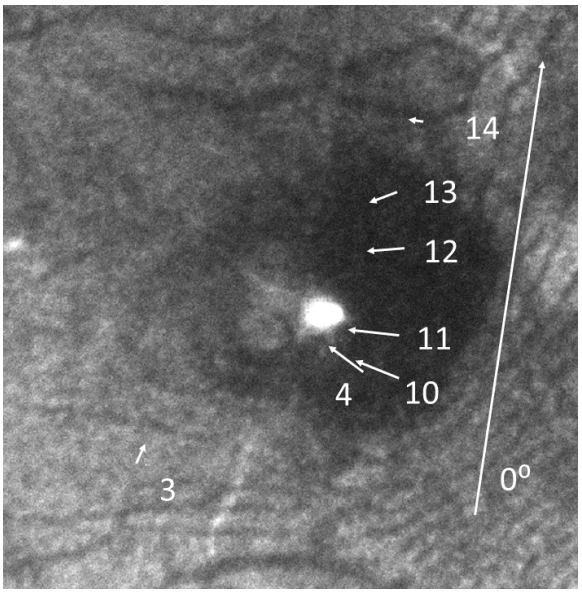

Figure 5.6: *The direction and magnitude of the tilt for the different positions close to the defocused part of the bump. The magnitude of the angle is shown by the length of the arrows, the direction of the tilt by the direction of the arrows. The direction where the angle equals zero is given by the large, white arrow. It is chosen such that the tilt on the measured positions is approximately pointing to the defocused part of the bump.*

5.2 Profile of collapsed material in a trench

As seen in section 3, the in-plane momentum of a reflected electron is dependent on the energy with which an electron comes in. The in-plane momentum is then imaged as position in diffraction space, so the position in diffraction space is also dependent on energy. To check this energy dependency, we took the diffraction picture of a sample at various energies.

5.2.1 Sample

We stamped a flake of $MoTe_2$ on a substrate of Si(100), which has a trench etched into it. The trench was etched using electron-beam lithography and reactive ion etching. It is prepared in the same way as the sample in section 5.1, with the difference that before transferring the $MoTe_2$ flake to the substrate, there is a trench etched in the substrate. In figure 5.7 there is an optical picture of this situation. The flake then collapsed into the trench, but it did not rip apart. A schematic picture of this is shown in figure 5.8. At the edges of the trench the flake makes an angle with the surface, while in the center of the trench and next to the trench it is flat.

5.2.2 Results

As seen before, a tilted part of the sample means a shift in diffraction space. In the case of a collapsed flake on a trench, there are two tilted parts: one on either side of the trench. Since the situation is approximately symmetric across the trench, we expect these angles to be approximately equal. The

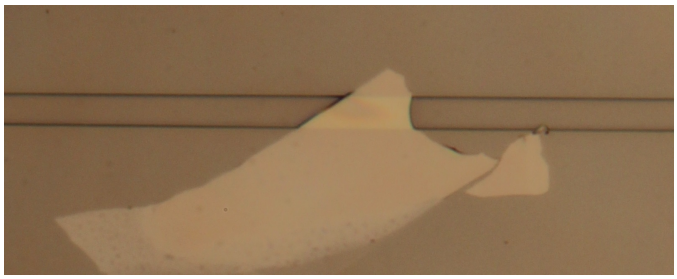

Figure 5.7: *Optical image of a flake of $MoTe_2$ on a Si(000) substrate with a trench in it.*

Figure 5.8: *Schematic drawing of a collapsed flake on a trench. The trench is drawn in black and the flake in red.*

diffraction pattern of this area is shown in figure 5.9. Instead of a single central spot, there is now a central spot with on the upper and lower side two satellites. The middle spot corresponds to the flat part of the surface. This consists of the flat parts in and next to the trench. Each of the satellite spots corresponds to the part of the flake on one of the sides of the trench as confirmed by μLEED measurements.

Figure 5.9: *The diffraction image of a collapsed flake of $MoTe_2$ on a trench. Contrast is inverted for clarity, the darkest spots have the highest intensity. The dark spots correspond to flat parts of the flake, the satellites above and below the dark spots correspond to the parts that have an angle. The red arrow corresponds to the distance that is plotted in figure 5.10.*

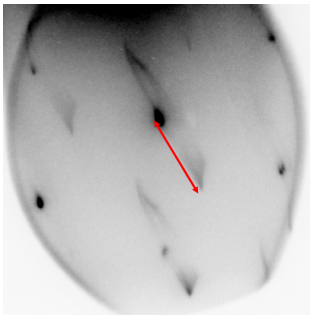

The position of these spots changes with energy. In figure 5.10 the distance between the central spot and the satellite spot on the lower right side (indicated in red in figure 5.9) are plotted as a function of energy. The distance grows as a function of energy. Fitting a power law to the data shows that the distance goes with energy to the power 0,21, with an error of 0,18.

From equation 3.4 it is expected that the in-plane momentum goes with the square root of energy. In the data this is not the case, it goes with $E^{0,2\pm0,18}$. The uncertainty in the exponent is relatively large, but not large

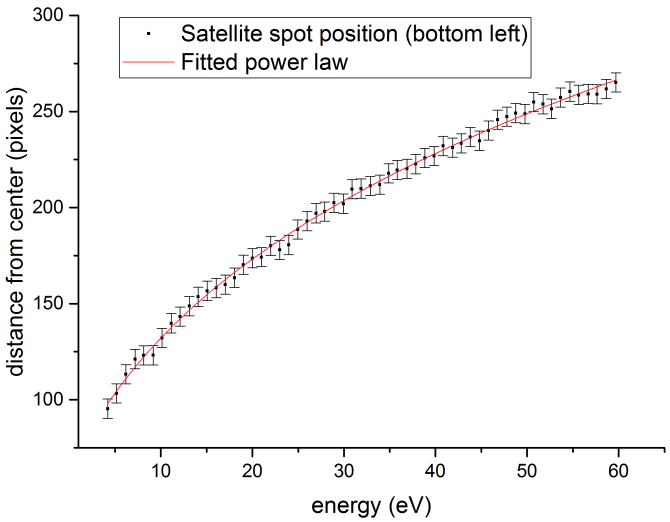

Figure 5.10: *The distance of the bottom left point of the bottom satellite spot to the central spot as a function of energy. Fitting a power law to the data points gives the relation* $distance \sim E^{0.21 \pm 0.18}$.

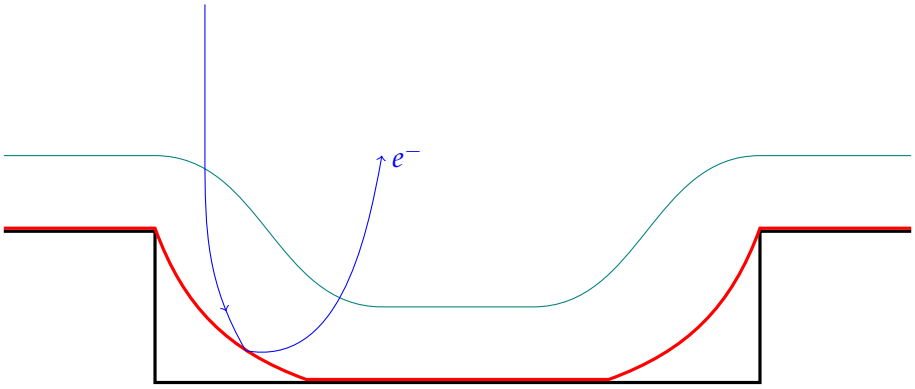

Figure 5.11: *Schematic drawing of the effect of lensing on the angle with which electrons reflect of a tilted sample. In blue the electron beam, only the specular reflected electron path is drawn. In red the sample and in green one of the equipotential lines.*

enough to justify an exponent of 0,5.

This can be explained because there are lensing effects. The potential landscape that slows down the electrons when they approach the sample is deformed around the trench. Since the surface is not flat, the potential is not only a function of distance from the sample, but also of position on the sample. This deflects the electrons and changes the angle with which they reach the sample.

In figure 5.11 the lensing effect is explained. Since there is a decelerating potential, the angle of incidence of the electrons gets bigger. That means the angle with which the electrons are reflected is also bigger. In diffraction space this larger angle leads to a larger distance from the original spot.

The next step is to correct for this energy dependence. Is is concluded

that the energy dependence follows the relation $\alpha \sim E^{0,2\pm0,18}$. Since the uncertainty in the exponent given by the fit in figure 5.10 is about as large as the exponent itself, the value of the exponent that removes the energy dependency needs to be found manually.

In figure 5.12 the angle is plotted after having corrected for energy, such that the energy dependency has vanished. When using an exponent of 0,39 for the energy dependency, a linear fit through the corrected data points gives a slope of 0,0005. From this we conclude that the exponent of 0,39 is correct. This is within the error margin of the fit in figure 5.10. This way the angle determination is also corrected for lensing.

By taking more measurements on the collapsed part of the flake, it would be possible to determine the distribution of angles over that part of the flake. From that the profile of the collapsed part of the flake could be calculated. Unfortunately we do not have enough measurements to calculate the profile here.

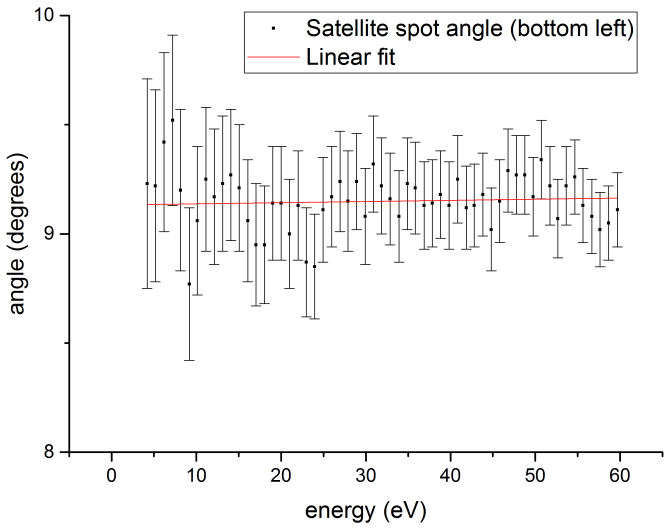

Figure 5.12: *The angles the flake makes at the edge of the trench after we corrected for energy. A linear fit was done on the angles to check if the angle is constant, which gave a slope of 0.0005.*

5.3 Discussion

The presented experiments show that the angle a material makes with its surroundings can be determined. The shift a spot gets in diffraction space due to the tilt of the material can be observed, and from that the angle a material has with the flat part of the surface can be calculated. By taking a set of measurements close to each other, the profile of a material can be deducted.

The main source of uncertainty in the angle determination is the error in determining the position of the diffraction spot. This leads to an uncertainty in angle of around 0.3°. The error is dependent on the energy

of the electrons. There are possibilities to improve the error in the position determination, which will be discussed in the outlook. The error also determines the resolution of our angle determination procedure. We can distinguish angles up to 0.3°.

The energy dependency of the angle determination procedure is calculated, but not yet completely explained. We see that lensing affects the angle with which electrons leave the sample. The effect of lensing can be taken out in the data analysis we do, but it would be good to rigorously calculate the electron paths in a potential that is created around a trench. We need to note though that the effects of lensing are strongly dependent on the surface profile of the sample. The effects of lensing need to be calculated per sample, to have an accurate idea of how lensing influences our measurements.

Chapter 6

Conclusion

In this work a method to determine the local surface profile of samples is described. The surface profile can be studied by looking at the local tilt angle on the surface of samples. By determining the local tilt angle at multiple positions a vector field of angles can be constructed. From that vector field the surface profile can be deduced.

The local tilt angle on a sample surface can be determined by analyzing a diffraction image. If there is an angle between two parts of the surface, this shows in diffraction as a shift of the complete pattern. Using the specular and first order spots as a gauge, the angle between the two parts of the surface can be calculated via

$$\alpha = \frac{1}{2} sin^{-1} \left(\frac{r_{shift}}{r_{1storder}} k_{\parallel 1storder} \frac{\hbar}{\sqrt{2mE}} \right).$$

The accuracy of this equation depends on the accuracy of the position determination of diffraction spots. The more smooth and small a spot is, the better the accuracy will be. We have tried to improve the resolution of the diffraction image, and by that lower the size of diffraction spots. It is not yet clear whether or not the deconvolution will improve the resolution; more work needs to be done on this.

The angle determination procedure is shown to work on two different samples. Angles can be determined to a precision of 0.3°. When the electronic potential field at the surface is not flat, for instance because of structures on the surface, lensing effects need to be taken into account. For a trench etched in the surface, this is shown to be possible.

Chapter 7

Outlook

7.1 Improving resolution by automatization of spot finding

In section 3.2 it is described that the accuracy with which the center of a spot can be determined limits the resolution of the angle determination. A way to improve the accuracy of determining the center of a spot is doing this automatized instead of manually.

If the position of every diffraction spot is determined in exactly the same way, the error that is in the human estimation of the position of a peak is eliminated. Automatizing the position finding procedure would also make it possible to handle larger data sets, extending the possibilities of the technique. In the examples mentioned in chapter 5 only a few angle measurements were taken. Both the density of points and the area covered can be increased when the spot finding is automatized.

Automatizing finding the position of a diffraction spot can be done by fitting the expected shape of a spot on the diffraction spot. The fitting procedure gives coordinates for the center of the spot. This should be more consistent and more precise than doing it by hand. There will still be an error in this since fitting on a non-smooth spot will be a bit imprecise. Also spots that deviate a lot from the standard shape of a diffraction spot will not be possible to fit.

For smooth spots though, automatizing the spot finding procedure can open up new possibilities [23].

7.2 Quantifying lensing effects

In section 5.2.2 it is described that the energy dependency of the angle with which electrons are reflected is not completely understood. It is possible to

compensate the energy effects, but we only have a qualitative explanation of the physics behind it.

Lensing effects happen close to the sample, because the potential landscape around a trench is not constant in the direction parallel to the surface. Qualitatively we can argue what the effect of lensing should be. Looking at the data, the explanation seems to match the data. To really understand the effect of lensing though, it is good to calculate the effects of the change in potential field rigorously. There is software for modelling electron optics, that could be useful for this.

Modelling the effect of a non-constant potential field on the electron paths would not only be useful for understanding what happens on our samples, but also for other experiments where lensing effects are seen. An example of such an experiment is imaging materials that are next to each other with different work functions, creating a step in potential at boundary as felt by the electrons.

Lensing effects are strongly dependent on the surface structure of samples. This dependency means that in principle the effects need to be calculated per sample. Some structures are used a lot, and those can be carried over per sample. The trenches we used consist for example of two step edges next to each other. The step edge is one of the most fundamental surface profile elements, and is used in a lot of different samples. A rigorous calculation of the electronic potential around a step edge would be useful in most of these samples.

7.3 Phase transitions in transition metal dichalcogenide monolayers

A specific subject where angle measurement in a LEEM can contribute, is the phase transition in transition metal dichalcogenide (TMD) monolayers. These materials consist of a layer of transition metal atoms, squeezed in between two layers of chalcogenide atoms. This structure of three sublayers is then called a TMD monolayer.

There are a few different crystal structures that TMD monolayers can have. The structure of a specific material is not fixed: by adding energy to the system it is possible to change the crystal structure. One way of doing this is by applying strain in the in-plane direction. Some materials, like $MoTe_2$, have a phase transition between two crystal structures already at 0.2 % strain.

A way to induce strain in a LEEM, is to place a monolayer of a TMD on a cavity, and then to put a voltage on the bottom of the cavity, creating a back-gate. The potential difference between the monolayer and the back-gate will create a force on the monolayer that pushes it outwards or pulls it inwards. Since the monolayer sticks to the surface of the sample by Van

der Waals-forces, it will not slip but the part of the monolayer on top of the cavity will strain. This is depicted in figure 7.1.

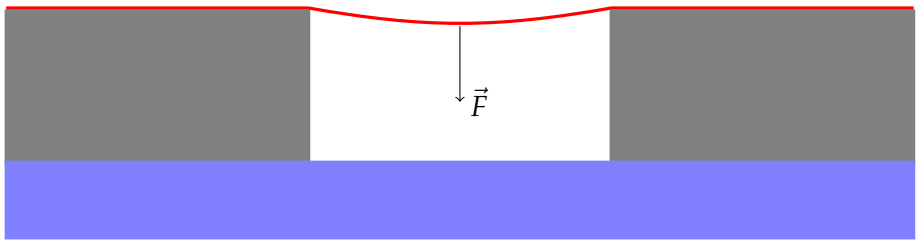

Figure 7.1: *Schematic drawing of a set up to induce strain in a monolayer. In red the monolayer and in blue the back gate that can be used to pull on the monolayer. The grey layer in between is an insulating substrate.*

To quantify the strain, angle measurement can be used. When the part of the monolayer on top of the cavity is pushed out, it will locally have an angle with the part of the flake next to the cavity. This angle can be determined using the procedure described in section 3. It is then possible to measure the relation between the strain in a TMD monolayer, and crystal structure it has.

Appendix

Appendix A

Derivation of the energy dispersion of tunneled electrons

In this section the derivation of the energy dispersion of electrons that tunneled out of an electron gun tip will be shown. We will follow the derivation for Cold Field Emission by Richard Forbes [24].

There are several factors influencing the electron energy dispersion when the electrons leave the gun tip. First we have the electrons arriving at the gun tip, described by Fermi-Dirac statistics, and the supply function, which describes the current density crossing a surface inside the metal. All these electrons then have a chance to tunnel through the potential barrier between the metal and the surrounding vacuum. The electrons that do tunnel then form the electron beam that is used in the electron microscope. In figure A.1 this process is drawn schematically. To be able to calculate the energy states in the gun tip we will assume in this derivation that the surface of the metal is perfectly flat. This is quite a strong assumption, but the resulting calculations give us a lot of insight in the shape of the energy distribution.

A.i The energy of the available electrons

The first step is to calculate the energy of the electrons that are available for tunneling. This is done using the supply function. The supply function describes the current density through a surface in a metal. Taking this surface to be the surface of the metal, the function describes the electrons available for tunneling out. Mathematically this is done by calculating the number of available states in k-space, then calculating the contribution from a single state and finally transform the result from k-space to energy space. This is then multiplied by the Fermi-Dirac distribution to use the correct occupa-

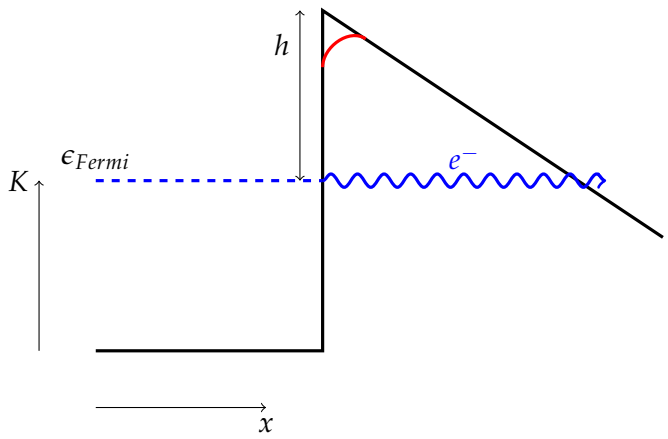

Figure A.1: *The most commonly used barrier shape: the triangular barrier, here drawn in black. In reality the top of the barrier is more rounded, which is indicated in red. On the x-axis is the distance in the direction perpendicular to the surface of the emitter, on the y-axis kinetic energy relative to the bottom of the conduction band of the emitter. The dotted blue line indicates the Fermi-level inside the emitter. The wiggly blue line is the electron tunneling through the barrier. The height of the barrier as seen by the electrons on the Fermi surface is called h.*

tion numbers for non-zero temperatures.

The first step is to calculate the number of electronic states per element in k-space. Since we assumed a flat surface of sufficient size, periodic boundary conditions can be used. The number of electronic states per element in k-space for an atomic lattice is given by

$$d^3n = \frac{2L^3}{(2\pi)^3} dk_x dk_y dk_z, \tag{A.1}$$

with $\left(\frac{2\pi}{L}\right)^3$ the size of a state in k-space [16]. Putting this in cylindrical coordinates (k_p, θ, k_z) with k_z the direction perpendicular to the emitter surface, $k_p = \sqrt{k_x^2 + k_y^2}$ the direction parallel to the emitter surface and integrating over the angle gives

$$d^2n = \frac{2L^3}{(2\pi)^3} dk_p dk_z \cdot \int_0^{2\pi} k_p d\theta, \tag{A.2}$$

$$= \frac{4\pi L^3 k_p}{(2\pi)^3} dk_p dk_z. \tag{A.3}$$

Each of the states in k-space contributes with its charge density normal to the emitter surface, which is the charge density in the state times the occupation number f_{FD} for that state. The charge density then needs to be multiplied with the velocity in the z-direction to get the current density.

The charge density in the state is given by $\frac{e}{L^3}$ and we denote the velocity in the z-direction by c_z. Multiplying this with equation A.3 yields the current density

$$d^2J = d^2n \cdot \frac{e}{L^3} f_{FD} c_z, \tag{A.4}$$

$$= \frac{4\pi e}{(2\pi)^3} f_{FD} k_p dk_p c_z dk_z. \tag{A.5}$$

The occupation number for a state is given by the Fermi-Dirac distribution. Putting this in then gives us the actual current density:

$$d^2J = \frac{4\pi e}{(2\pi)^3} \cdot \frac{1}{\exp((\epsilon)/k_B T) + 1} k_p dk_p c_z dk_z. \tag{A.6}$$

Here ϵ is defined as the energy of an electron relative to the Fermi-energy. Equation A.6 can be converted to an expression in energy differentials instead of k-differentials. Since we use a free-electron model, the energy of the electrons is only kinetic energy. We will define the total energy of the electrons as the kinetic energy relative to the bottom of the conduction band. This energy K can be expressed as a function of k_z and k_p via

$$K = \frac{\hbar^2}{2m}(k_z^2 + k_p^2). \tag{A.7}$$

Similarly, the parallel component of the kinetic energy is given by

$$K_p = \frac{\hbar^2}{2m} k_p^2, \tag{A.8}$$

and the z-component by

$$K_z = \frac{\hbar^2}{2m} k_z^2 = K - K_p. \tag{A.9}$$

The differentials are then given by

$$dK_p = \frac{\hbar^2}{2m} k_p dk_p, \tag{A.10}$$

$$dK_z = \frac{\partial K}{\partial k_z} dk_z, \tag{A.11}$$

since K_p is independent on k_z.

Finally c_z can be expressed in these differentials. Since the electron is a quantum mechanical wave we can interpret c_z as a group velocity. It is known that for a group velocity with angular frequency ω

$$c_z = \frac{\partial \omega}{\partial k_z}, \tag{A.12}$$

$$K = \hbar\omega, \tag{A.13}$$

from which follows that

$$c_z = \frac{1}{\hbar}\frac{\partial K}{\partial k_z}. \tag{A.14}$$

Putting equations A.10, A.11 and A.14 into equation A.6 then yields

$$d^2J = \frac{4\pi em}{h^3} \cdot \frac{1}{\exp((\epsilon)/k_BT)+1} dK_p dK_z. \tag{A.15}$$

For a constant value of K_p, $dK_z = dK$ holds. Since we assumed free-moving electrons, furthermore $dK = d\epsilon$ with ϵ the total energy relative to the Fermi energy. Combining this gives

$$d^2J = \frac{4\pi em}{h^3} \cdot \frac{1}{\exp((\epsilon)/k_BT)+1} dK_p d\epsilon, \tag{A.16}$$

$$= z_S f_{FD} dK_p d\epsilon, \tag{A.17}$$

where z_S is Sommerfeld's electron supply constant and f_{FD} is the Fermi-Dirac distribution.

A.ii Tunneling through the potential barrier

Equation A.17 yields the charge density arriving at the surface of the gun tip, but not all these electrons actually leave the tip. They have to tunnel through the potential barrier, which goes with a certain probability D. The final energy distribution is then equation A.17 times D.

This parameter D depends on the energy of the electron and the shape and height of the barrier it has to tunnel through. To exactly calculate the escape probability of the electron, a Schrödinger equation needs to be solved. This is not always possible to do analytically, depending on the shape of the barrier. The simplest case, a triangular barrier, can be analytically solved and is used as a basis for approximating other shapes. The triangular barrier is shown in figure A.1. We will use a triangular barrier in the following calculations.

This is an approximation of the true form of the potential in cold emission, but quite a good one since the region in which the potential of the work function is felt is typically in the order of an inter atomic distance. The external field though works on much greater distances, so the part of the barrier which is actually curved is very small.

The calculation of D now takes place in two steps: first it is expressed in the unreduced barrier height h, which can be interpreted as the height of the barrier as seen by an electron relative to its own energy. Next this h is converted to ϵ and K_p.

We define h as

$$h = \phi - \epsilon + K_p, \tag{A.18}$$

with ϕ the work function. Equation A.18 says that the reduced barrier height is the work function, or the barrier height relative to the Fermi level, minus the energy of the electron perpendicular to the surface of the emitter. Since this describes a tunneling process we know that D should be an exponentially declining function of h. That means that it can be described by

$$D(h) = \exp[-G(h)], \tag{A.19}$$

where $G(h)$ is called the Gamow exponent. The exact shape $G(h)$ takes depends on the shape of the barrier. $G(h)$ can be Taylor expanded around ϕ since the electron energy relative to the barrier height is small:

$$\begin{aligned} G(h) &\simeq G(\phi + \delta h), && \text{(A.20)} \\ &= G_F + \frac{\partial G}{\partial h}\delta h + \dots, && \text{(A.21)} \\ &= G_F + \frac{\delta h}{d_F} + \dots, && \text{(A.22)} \end{aligned}$$

where d_F is defined via

$$d_F^{-1} \equiv \frac{\partial G}{\partial h}, \tag{A.23}$$

and expresses the sensitivity of the tunnel probability on a change in the barrier height. Putting this into equation A.19 yields

$$D \simeq D_F \exp\left(-\frac{\delta h}{d_F}\right). \tag{A.24}$$

The label F on the parameters signal that these outcomes are only valid for electron energies close to the Fermi surface.

From equation A.18 it follows that

$$\begin{aligned} \delta h &= \left.\frac{\partial h}{\partial \epsilon}\right|_{K_p} \delta\epsilon + \left.\frac{\partial h}{\partial K_p}\right|_{\epsilon} \delta K_p, && \text{(A.25)} \\ &= -\delta\epsilon + \delta K_p. && \text{(A.26)} \end{aligned}$$

For an electron at the Fermi energy that is normally incident on the emitter surface $\epsilon = 0$ and $K_p = 0$ hold, and D can be expressed as

$$D \simeq D_F \exp\left(\frac{\epsilon}{d_F}\right) \exp\left(-\frac{K_p}{d_F}\right), \tag{A.27}$$

where D_F and d_F are determined by the shape of the barrier.

Combining approximation A.27 with equation A.17 and integrating over K_p, the kinetic energy parallel to the emitter surface, gives an expression for the current density coming out of the emitter as a function of the electron

energy. The integration runs over all electron energies in the conduction band:

$$j(\epsilon) = z_S f_{FD} D_F \exp\left(\frac{\epsilon}{d_F}\right) \cdot \int_0^{K_F+\epsilon} \exp\left(-\frac{K_p}{d_F}\right) dK_p. \tag{A.28}$$

Evaluating this integral gives

$$j(\epsilon) = z_S f_{FD} d_F D_F \left[\exp\left(\frac{\epsilon}{d_F}\right) - \exp\left(-\frac{K_F}{d_F}\right)\right]. \tag{A.29}$$

For a metal it is known that the conduction band is large, which means that the energy of the Fermi-level relative to the bottom of the conduction band K_F is large. d_F is called the decay width and describes the sensitivity of the tunneling probability on a change of the barrier height. Since the tunneling probability depends exponentially on the barrier height, a small change in energy has a large effect on the tunneling probability. We can thus conclude that d_F is small, while K_F is big. Forbes concludes from this that the second exponential in equation A.29 can be neglected [24]. The equation then becomes

$$j(\epsilon) = z_S f_{FD} d_F D_F \exp\left(\frac{\epsilon}{d_F}\right), \tag{A.30}$$

and we have a result in which a barrier shape can be inserted.

To evaluate this, $G(h)$ has to be known. This can be a very complex quantum mechanical problem, so it is a good idea to use an approximation here. Wentzel, Kramers and Brillouin found out that it is possible to approximate the wave function of a particle when it is in a sufficiently slowly changing potential. An expansion of the wave function of a particle in a constant potential will be a good approximation in that case [25] [26] [27]. This is called the WKB-approximation.

This makes the wave function much more easy to calculate since the exact solution of a particle in a constant potential with $V < \epsilon$ is known to be

$$\Psi = \exp\left(\frac{ipx}{\hbar}\right), \tag{A.31}$$

where $p = \sqrt{2m(\epsilon - V)}$. Here V is defined relative to the Fermi-level. We will now follow the derivation of David Bohm [28] to get to the transmission coefficient D. First we approximate the wave function with

$$\Psi = \exp\left(\frac{iS}{\hbar}\right), \tag{A.32}$$

with S being a function of x. If V would be constant S would be px, but to do this for a non-constant V, S is approximated as a series of powers in $\hbar$:

$$S = S_0(x) + \hbar S_1(x) + \frac{\hbar^2}{2} S_2(x) + \dots. \tag{A.33}$$

Equation A.32 can now be put in the time-independent Schrödinger equation and S substituted with equation A.33. Solving it then yields

$$\begin{aligned}\Psi =& \frac{A}{\sqrt[4]{\epsilon - V(x)}} \exp\left[i \int_{x_0}^{x} \sqrt{2m(\epsilon - V)} \frac{dx}{\hbar} \right] \\ &+ \frac{B}{\sqrt[4]{\epsilon - V(x)}} \exp\left[-i \int_{x_0}^{x} \sqrt{2m(\epsilon - V)} \frac{dx}{\hbar} \right],\end{aligned} \tag{A.34}$$

which is a superposition of a wave moving in the positive direction and one moving in the negative direction. Equation A.34 reduces to the plane waves $\exp(ipx/\hbar)$ and $\exp(-ipx/\hbar)$ in the case that V is constant.

This can be applied to the penetration of a potential barrier. We calculate the amplitude of the wave function on both sides of the barrier, and then the ratio of these amplitudes will be the penetration probability. The constants A and B need to be determined for this. They depend on the wave function inside the barrier, which can also be calculated within the WKB approximation, but with $V > \epsilon$. In this case the solution consists of real exponentials:

$$\begin{aligned}\Psi =& \frac{C}{\sqrt[4]{2m(\epsilon - V)}} \exp\left[\int_{x_0}^{x} \sqrt{2m(V - \epsilon)} \frac{dx}{\hbar} \right] \\ &+ \frac{D}{\sqrt[4]{2m(\epsilon - V)}} \exp\left[- \int_{x_0}^{x} \sqrt{2m(V - \epsilon)} \frac{dx}{\hbar} \right].\end{aligned} \tag{A.35}$$

The solutions inside and outside the barrier now need to be connected. This is not trivial, since the WKB approximation is not valid around the turning points of the barrier. The turning points are the points where the energy of the electrons is equal to the barrier height ($\epsilon = V$), which leads to dividing by 0 at these points (see figure A.1). There is however a trick to solve this. If the region where the WKB approximation does not apply is small enough, it can be approximated with a straight line. In that case, Schrödinger's equation looks like

$$-\frac{\hbar^2}{2m} \frac{\partial^2 \Psi}{\partial x^2} + C(x - a)\Psi = 0, \tag{A.36}$$

with $C = (\partial V / \partial x)_{x=a}$. Equation A.36 can be solved using Bessel's functions of order ⅓. I will only quote the results here, for the complete procedure see the article by R.E. Langer on this [29]. Connecting the left, middle and right part of the wave function and taking the ratio of the left and right part then yields

$$D = \exp\left(-2 \int_{a}^{b} \sqrt{2m(V - \epsilon)} \frac{dx}{\hbar} \right), \tag{A.37}$$

which can be rewritten as

$$D = \exp\left(-g_e \int U^{1/2} dx\right), \tag{A.38}$$

with

$$g_e \equiv \sqrt{8m}/\hbar, \tag{A.39}$$
$$U \equiv V - \epsilon. \tag{A.40}$$

Here g_e is a constant for electron tunneling and U is an energy-like quantity which expresses the height of the barrier relative to the energy of an electron. Comparing this to equation A.19 it can be seen that

$$G(h) = g_e \int U^{1/2} dx. \tag{A.41}$$

Now we can put in the shape of the triangular barrier. For a triangular barrier U can be expressed as

$$U = h - eFx, \tag{A.42}$$

with F the strength of the applied field. Putting this in equation A.41 yields

$$G_{tr}(h) = \frac{bh^{3/2}}{F}, \tag{A.43}$$

with

$$b = \frac{2}{3e} g_e. \tag{A.44}$$

Now it follows from equations A.19, A.23 and A.43 that

$$D_F^{tr} = \exp\left(-\frac{b\phi^{3/2}}{F}\right), \tag{A.45}$$
$$d_F^{tr} = \frac{2}{3b}\phi^{-1/2} F. \tag{A.46}$$

These results we can then put into equation A.30. This gives

$$j(\epsilon) = z_S f_{FD} \frac{2F}{3b\phi^{1/2}} \exp\left(\frac{b\phi^{1/2}(3\epsilon/2 - \phi)}{F}\right), \tag{A.47}$$

which describes the energy dispersion of the electrons that have tunneled out of the emitter.

Bibliography

[1] K. S. Novoselov, A. K. Geim, S. V. Morozov, D. Jiang, Y. Zhang, S. V. Dubonos, I. V. Grigorieva, and A. A. Firsov, *Electric Field Effect in Atomically Thin Carbon Films*, Science **306**, 666 (2004).

[2] AlexanderAIUS, 2010, url:https://commons.wikimedia.org/wiki/File:Graphen.jpg, retrieved November 25 2017. Reprinted under Creative Commons Attribution-Share Alike 3.0 Unported license.

[3] G. Lalwani, A. Henslee, B. Farshid, L. Lin, F. Kasper, Y. Qin, A. Mikos, and B. Sitharaman, *Two-Dimensional Nanostructure-Reinforced Biodegradable Polymeric Nanocomposites for Bone Tissue Engineering*, Biomacromolecules **14**, 900 (2013).

[4] D. Overbye, *Reaching for the Stars, Across 4.27 Light-Years*, New York Times (2016), Retrieved November 20 2017.

[5] A. Geim and K. Novoselov, *The Rise of Graphene*, Nature Materials **6**, 183 (2007).

[6] S. Lee, K. Lee, C. Liu, G. Kulkarni, and Z. Zhong, *Flexible and Transparent All-Graphene Circuits for Quaternary Digital Modulations*, Nature Communications **3** (2012).

[7] K. Duerloo, Y. Li, and E. Reed, *Structural Phase Transitions in Two-Dimensional Mo- and W-Dichalcogenide Monolayers*, Nature Communications **5**, 1 (2014).

[8] J. Bardeen, *Surface States and Rectification at a Metal Semi-Conductor Contact*, Physical Review **71**, 717 (1947).

[9] R. Kappere, D. Voiry, S. Yalcin, W. Jen, M. Acerce, S. Torrel, B. Branch, S. Lei, W. Chen, S. Najmaei, J. Lou, P. Ajayan, G. Gupta, A. Mohite, and M. Chhowalla, *Metallic 1T Phase Source/Drain Electrodes for Field*

Effect Transistors from Chemical Vapor Deposited MoS2, APL Materials **2** (2014).

[10] S. Song, D. Keum, S. Cho, D. Perello, Y. Kim, and Y. Lee, *Room Temperature Semiconductor-Metal Transition of MoTe2 Thin Films Engineered by Strain*, Nano Letters **16**, 188 (2016).

[11] A. Castellanos-Gomez, R. Van Leeuwen, M. Buscema, H. S. J. Van Der Zant, G. A. Steele, and W. J. Venstra, *Single-Layer MoS2 Mechanical Resonators*, Advanced Materials **25**, 6719 (2013).

[12] S. Schramm, *Imaging with Aberration-Corrected Low Energy Electron Microscopy*, PhD thesis, Universiteit Leiden, 2013.

[13] S. Tanuma, C. Powell, and D. Penn, *Calculations of Electron Inelastic Mean Free Paths. V. Data for 14 Organic Compounds over the* 50 *to* 2000 eV *Range*, Surface and Interface analysis **21** (1994).

[14] R. M. Tromp, J. B. Hannon, A. W. Ellis, W. Wan, A. Berghaus, and O. Schaff, *A new aberration-corrected, energy-filtered LEEM/PEEM instrument. I. Principles and design*, Ultramicroscopy **110**, 852 (2010).

[15] S. Schramm, J. Kautz, A. Berghaus, O. Schaff, R. Tromp, and S. van der Molen, *Low-Energy Electron Microscopy and Spectroscopy with ESCHER: Status and Prospects*, IBM Journal of Research and Development **55** (2011).

[16] C. Kittel, *Introduction tot Solid State Physics*, John Wiley & Sons, New York, 1976.

[17] G. Binnig, H. Rohrer, C. Gerber, and E. Weibel, *Reconstruction on Si(111) Resolved in Real Space*, Phys. Rev. Lett. **50**, 120 (1983).

[18] J. Kautz, unpublished, 2013.

[19] A. Roosenbrand, *High-Resolution Low-Energy Electron Diffraction*, PhD thesis, Technische Universiteit Eindhoven, 1990.

[20] K. Gronwald and M. Henzler, *Epitaxy of Si(111) as Studied With a New Resolving LEED System*, Surface Science **117**, 180 (1982).

[21] R. Forbes, *Gas Field Ionization Sources*, in *Handbook of Charged Particle Optics*, edited by J. Orloff, chapter 3, pages 87–128, CRC Press, Boca Raton, Florida, USA, 1997.

[22] R. Fowler and L. Nordheim, *Electron Emission in Intense Electric Fields*, in *Proceedings of the Royal Society of London. Series A, Containing Papers of a Mathematical and Physical Character*, volume 119, pages 173–181, The Royal Society, 1928.

[23] A. van der Torren, *Growing Oxide Thin Films in a Low-Energy Electron Microscope*, PhD thesis, Universiteit Leiden, 2016.

[24] R. Forbes, *Use of Energy-Space Diagrams in Free-Electron Models of Field Electron Emission*, Surface and Interface Analysis , 395 (2004).

[25] G. Wentzel, *Eine Verallgemeinerung der Quantenbedingungen für die Zwecke der Wellenmechanik*, Zeitschrift fur Physik **38**, 518 (1926).

[26] H. Kramers, *Wellenmechanik und halbzahlige Quantisierung*, Zeitschrift fur Physik **39**, 828 (1926).

[27] L. Brillouin, *La Mécanique Ondulatoire de Schrödinger: une Méthode Générale de Resolution par Approximations Successives*, Comptes Rendus de l'Académie des Sciences **183**, 24 (1926).

[28] D. Bohm, *Quantum Theory*, Prentice-Hall, Inc., Englewood Cliffs, N.J., U.S.A., 1951.

[29] R. Langer, *On the Connection Formulas and the Solutions of the Wave Equation*, Phys. Rev. **51** (1937).